

Unique high-energy excitons in two-dimensional transition metal dichalcogenides

Yongsheng Gao(高永盛), Yuanzheng Li(李远征), Weizhen Liu(刘为振), Chuxin Yan(闫楚欣), Qingbin Wang(王庆彬), Wei Xin(辛巍), Haiyang Xu(徐海阳), and Yichun Liu(刘益春)
Citatio: Chin. Phys. B, 2025, 34 (**9**): 097102. DOI: 10.1088/1674-1056/ade074
http://cpb.iphy.ac.cn; http://iopscience.iop.org/cpb

What follows is a list of articles you may be interested in

Anomalous ultrafast thermalization of photoexcited carriers in two-dimensional materials induced by orbital coupling

Zhuoqun Wen(文卓群), Haiyu Zhu(诸海渝), Wen-Hao Liu(刘文浩), Zhi Wang(王峙), Wen Xiong(熊稳), and Xingzhan Wei(魏兴战)
Chin. Phys. B, 2025, 34 (**7**): 077103. DOI: 10.1088/1674-1056/adc191

Unveiling the thermal transport mechanisms in novel carbon-based graphene-like materials using machine-learning potential

Yao-Yuan Zhang(章耀元), Meng-Qiu Long(龙孟秋), Sai-Jie Cheng(程赛杰), and Wu-Xing Zhou(周五星)
Chin. Phys. B, 2025, 34 (**6**): 067101. DOI: 10.1088/1674-1056/adca18

High-temperature ferromagnetism and strong π-conjugation feature in two-dimensional manganese tetranitride

Ming Yan(闫明), Zhi-Yuan Xie(谢志远), and Miao Gao(高淼)
Chin. Phys. B, 2023, 32 (**3**): 037104. DOI: 10.1088/1674-1056/acae7b

Two ultra-stable novel allotropes of tellurium few-layers

Changlin Yan(严长林), Cong Wang(王聪), Linwei Zhou(周霖蔚), Pengjie Guo(郭朋杰), Kai Liu(刘凯), Zhong-Yi Lu(卢仲毅), Zhihai Cheng(程志海), Yang Chai(柴扬), Anlian Pan(潘安练), Wei Ji(季威)
Chin. Phys. B, 2020, 29 (**9**): 097103. DOI: 10.1088/1674-1056/aba606

Effects of layer stacking and strain on electronic transport in two-dimensional tin monoxide

Yanfeng Ge(盖彦峰), Yong Liu(刘永)
Chin. Phys. B, 2019, 28 (**7**): 077104. DOI: 10.1088/1674-1056/28/7/077104

TOPICAL REVIEW — Exciton physics: Fundamentals, materials and devices

Unique high-energy excitons in two-dimensional transition metal dichalcogenides

Yongsheng Gao(高永盛), Yuanzheng Li(李远征)[†], Weizhen Liu(刘为振), Chuxin Yan(闫楚欣), Qingbin Wang(王庆彬), Wei Xin(辛巍), Haiyang Xu(徐海阳)[‡], and Yichun Liu(刘益春)[§]

State Key Laboratory of Integrated Optoelectronics, and Key Laboratory of UV-Emitting Materials and Technology of Ministry of Education, Northeast Normal University, Changchun 130024, *China*

(Received 26 April 2025; revised manuscript received 1 June 2025; accepted manuscript online 4 June 2025)

Two-dimensional (2D) transition metal dichalcogenides (TMDs), endowed with exceptional light–matter interaction strength, have become a pivotal platform in advanced optoelectronics, enabling atomically precise control of excitonic phenomena and offering transformative potential for engineering next-generation optoelectronic devices. In contrast to the narrowband absorption characteristics of conventional band-edge excitons, which are limited by the bandgap energy, high-energy excitons not only demonstrate broad momentum matching capability in the ultraviolet regime due to band nesting effects, but also exhibit distinct absorption peak signatures owing to robust excitonic stabilization under 2D confinement. These unique photophysical properties have established such systems as a prominent research frontier in contemporary exciton physics. This review primarily outlines the distinctive physical characteristics of high-energy excitons in TMDs from the perspectives of band structure, excitonic characteristics, and optical properties. Subsequently, we systematically delineate cutting-edge developments in TMD-based photonic devices exploiting high-energy excitonic band-nesting phenomena, with dedicated emphasis on the strategic engineering of nanoscale heterostructures for tailored optoelectronic functionality. Finally, the discussion concludes with an examination of the challenges associated with the design of high-energy exciton devices and their potential future applications.

Keywords: two-dimensional materials, transition metal dichalcogenides, high-energy excitons, band nesting effect, optoelectronic applications

PACS: 71.35.–y, 73.63.–b, 71.35.Cc, 71.35.Pq

DOI: 10.1088/1674-1056/ade074 **CSTR:** 32038.14.CPB.ade074

1. Introduction

The discovery of mechanically exfoliated graphene constitutes a pivotal milestone in materials science, unveiling the extraordinary realm of two-dimensional (2D) layered systems.[1] Over subsequent decades, the development of this family of atomically thin materials has profoundly impacted modern materials science, garnering extensive scientific interest due to their unique fundamental physical properties.[2–4] These layered structures are primarily maintained by weak van der Waals interactions along the out-of-plane direction, enabling precise atomic-scale engineering. This unique advantage has propelled fundamental discoveries from correlated electron physics to quantum light–matter interactions. Among them, 2D transition metal dichalcogenides (TMDs, MX_2: M = Mo, W, etc.; X = S, Se, etc.) have emerged as a cornerstone semiconductor class, exhibiting extraordinary layer-number-dependent electronic structure reconfiguration. In their bulk form, TMDs typically behave as indirect bandgap semiconductors, whereas quantum confinement effects and the splitting of valley degeneracy states induced by broken inversion symmetry in monolayer configurations induce a dramatic transition to direct bandgap characteristics.[5] This thickness-tunable bandgap engineering, coupled with strong spin–orbit coupling and valley-polarized excitons, has established monolayer TMDs as a versatile platform for next-generation optoelectronics, valleytronic devices, and quantum light emission systems.[6–8] Investigations into the excitonic properties in 2D TMDs have become a foundational element for the advancement of next-generation optoelectronics, offering unprecedented opportunities to engineer ultrafast-response, high-efficiency optoelectronic devices. Compared to their three-dimensional counterparts, the extreme quantum confinement and reduced dielectric screening in monolayer TMDs generate extraordinary Coulomb interactions, yielding exciton binding energies exceeding several hundred millielectron Volts (meV) that are two orders of magnitude greater than those in conventional semiconductors (e.g., GaAs: $\sim$ 10 meV).[9] These remarkable attributes not only enable room-temperature exciton stability but also establish 2D TMDs as a pioneering experimental platform for exploring exciton physics and related ap-

[†]Corresponding author. E-mail: liyz264@nenu.edu.cn
[‡]Corresponding author. E-mail: hyxu@nenu.edu.cn
[§]Corresponding author. E-mail: ycliu@nenu.edu.cn

© 2025 Chinese Physical Society and IOP Publishing Ltd. All rights, including for text and data mining, AI training, and similar technologies, are reserved.

plications at the 2D limit.[10,11] The excitonic landscape in the 2D TMDs unveils a diverse array of physical characteristics, bearing significant technological ramifications. For instance, valleytronic studies originate from valley-polarized exciton states induced by strong spin–orbit coupling (SOC).[12,13] The exciton dynamics in these materials encompass various many-body states, including interlayer excitons,[14–17] charged excitons (trions),[18] and dark excitons.[19,20] Furthermore, these systems exhibit intricate interactions, such as exciton–phonon coupling[21,22] and strong coupling effects between excitons and plasmons.[23–26] This confluence of robust exciton resilience and programmable quantum interactions positions 2D TMDs at the vanguard of both fundamental quantum material research and applied optoelectronic applications. 2D TMDs have become an ideal platform for studying quantum interactions due to their unique structural flexibility and tunable quantum effects. In the context of band engineering and electronic state modulation, both layer stacking and heterostructure configurations enable precise design of bandgap types and widths, while vertical electric fields facilitate effective modulation of band alignment. These strategic approaches significantly influence exciton formation and carrier transport properties. The strong SOC of two-dimensional TMDs leads to band spin splitting. Through valley-selective optical excitation and reasonable material structure design, it is conducive to achieving the manipulation of spin polarization.

In recent years, high-energy excitons have emerged as a particularly compelling research frontier in the study of excitonic properties in 2D TMDs, thanks to their transition dipole moment and strong coupling characteristics with the ultraviolet band's intense optical field. These high-energy excitons typically originate from transitions involving higher energy bands (e.g., those near the Γ-point), exhibiting energy ranges of 2.5 to 3.0 eV — a range that significantly exceeds those of band-edge A and B excitons ($\sim$ 1.8–2.0 eV).[27,28] High-energy excitons not only exhibit significant high-energy optical transitions but also serve as a source of high photoconductivity in 2D TMDs. Early theoretical calculations revealed that such high-energy transitions are intrinsically linked to the unique band nesting structure.[29] The band nesting structure endows the joint density of states (JDOS) with the characteristics of van Hove singularities (VHS).[30] The parallelism of the conduction and valence bands in momentum space enhances the correlation between electron–hole pairs, thereby significantly increasing the JDOS over a wide range of momenta. High-energy excitons in 2D TMDs predominantly reside within the visible to near-ultraviolet spectral range, effectively extending the optical absorption capabilities of TMDs materials. This combination of high-energy excitation and broadband absorption properties is of great significance for the design of high-efficiency UV photodetectors and solar energy harvesting devices, and is conducive to further optimization of the light absorption efficiency of high-energy excitations to achieve photon capture performance close to the theoretical limit.[31–37] Furthermore, their strong nonlinear optical responses, including second-harmonic generation and two-photon absorption, position them as promising candidates for next-generation ultrafast photonic modulators.[38,39] Since strain sensitivity and the resonance effect of high-energy excitons are tightly linked, strain-detection methods based on high-energy excitons have a lot of promise for flexible electronic devices and nanoscale mechanical measurements. As a novel high-energy quantum state in 2D systems, the study of high-energy excitons is not only a deepening of many-body physics in low-dimensional materials, but also a key bridge connecting optoelectronics, quantum technology and energy conversion applications. While recent years have witnessed substantial progress in experimental observations and theoretical interpretations of high-energy excitons in 2D TMDs, comprehensive reviews systematically evaluating current research achievements and practical applications remain notably scarce. A significant gap still exists: there is no systematic framework linking the ultrafast dynamics of high-energy excitons (such as inter-excitonic energy transfer, defect-mediated localization, and hot carrier relaxation) to their revolutionary uses in energy conversion systems, photonic devices, and strain sensing. Such critical analyses are urgently required to consolidate existing knowledge, identify unresolved challenges, and guide future explorations in this rapidly evolving field.

In this review, we systematically summarize recent advancements in the fundamental properties and applications of high-energy excitons in 2D TMDs, with comprehensive discussions focusing on their band structures, intrinsic excitonic characteristics, modulation strategies, and optoelectronic implementations. The review is organized as follows. Initially, we consolidate and analyze the band characteristics, optical absorption mechanisms, and nonlinear optical phenomena associated with high-energy excitons in 2D TMDs. Following this, we review investigations into exciton dynamics involving high-energy states, encompassing critical processes such as hot carrier relaxation/extraction, energy transfer between high-energy and band-edge excitons, and defect-mediated relaxation pathways. This section concludes with an overview of high-energy exciton resonance characteristics revealed through Raman scattering spectroscopy. Subsequently, the review extensively examines four emerging application domains enabled by high-energy exciton engineering: 1) high-performance optoelectronic devices; 2) nanoscale strain sensing platforms; 3) energy/charge transfer for enhanced quantum yield of band-edge excitons; and 4) quantum light manipulation technologies. Finally, we present critical perspectives on the current limitations of research in this field and

potential future directions for development. By synthesizing cutting-edge experimental findings and application breakthroughs, this work aims to provide researchers engaged in high-energy exciton studies with an updated framework for understanding fundamental mechanisms, technological potentials, and interdisciplinary connections. The systematic compilation of these advances serves not only as a technical reference but also stimulates innovative approaches for harnessing high-energy excitonic phenomena in next-generation quantum and optoelectronic systems.

2. Characteristics of high-energy excitons in 2D TMDs

2.1. The energy band structure of high-energy excitons

In common semiconducting 2D TMDs such as MoS_2, WS_2, and WSe_2, the trigonal prismatic (2H) phase represents a thermodynamically stable hexagonal crystal structure. This configuration features an ABA stacking sequence of sulfur-metal-sulfur trilayers (Fig. 1(a)).[40] The quantum degrees of freedom inherent in this structure endow the Brillouin zone with distinctive valley characteristics, where the valley physics at the zone edges is governed by spin-selective $+K$ and $-K$ valleys (Fig. 1(b)).[41] Figure 1(b) illustrates the layer-dependent band structure evolution of 2H-phase MoS_2, demonstrating a critical transition from indirect bandgap behavior in bulk crystals to direct bandgap characteristics in monolayers. In monolayer configurations, both the conduction band minimum and the spin–orbit-split valence band maximum converge at the K-point, highlighting the significant influence of interlayer interactions on the electronic structure of 2D TMDs semiconductors.

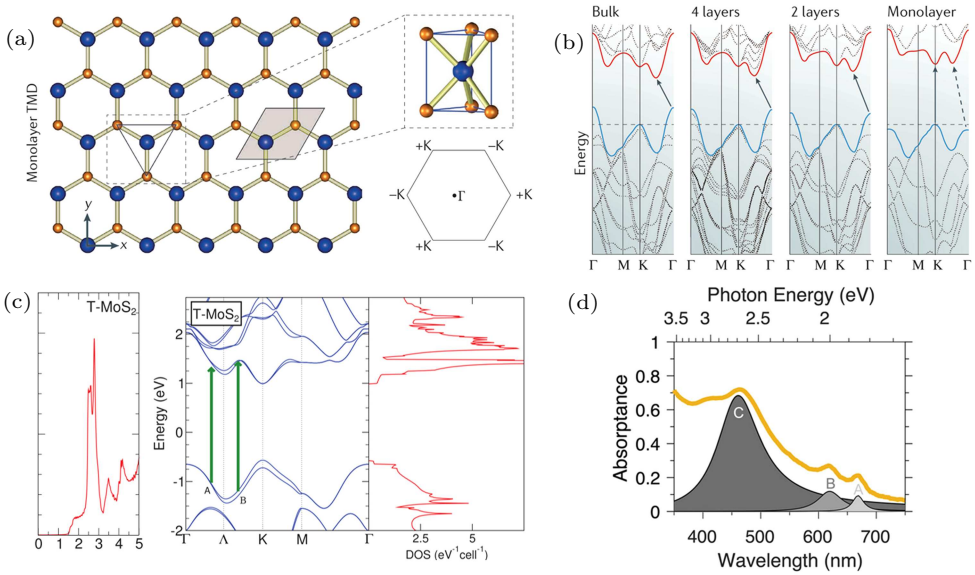


Fig. 1. (a) Top-view schematic of the hexagonal crystal structure of monolayer TMDs. Blue and orange spheres represent transition metal (M) and chalcogen (X) atoms, respectively. The triangular inset indicates the cross-sectional atomic arrangement. The first Brillouin zone is labeled with the Γ point and two inequivalent high-symmetry momentum points ($+K$ and $-K$).[40] (b) The variation in the band structure of MoS_2 with the change in layer number from bulk to monolayer.[41] (c) The variation diagram of optical conductivity for MoS_2 with a triangular prismatic structure, along with the corresponding energy band structure and density of states (DOS).[29] (d) The absorption spectrum of few-layer MoS_2 on 40 nm Ag glass.[47]

The remarkable light–matter interaction in 2D TMDs manifests as strong optical absorption across ultraviolet and visible spectral ranges. Theoretical investigations reveal that this phenomenon fundamentally arises from the synergistic interaction between excitonic states (electron–hole bound states) and band nesting effects in high-energy regions of the band structure.[29,42] The energy band nesting effect is the existence of parallel regions in momentum space (where the energy difference gradient approaches zero), causing electrons and holes to share identical group velocities with opposite directions, which significantly increases the JDOS and triggers singularities (divergences) in optical conductivity. These are manifested as strong and broad absorption peaks in the optical absorption spectrum. In contrast, D excitons occupy higher-energy shoulders of C excitons, exhibiting distinct non-parallel band characteristics.[43,44] As shown in Fig. 1(c), the 2H-phase MoS_2 displays pronounced band nesting regions along the Γ–M–K path,[29] where strong parallelism between conduction and valence bands generates intense optical conductivity peaks in the 2.5–3 eV range. The C excitons in these nesting regions primarily comprise six nearly degenerate excitonic states, forming a hexagonally symmetric ring near the Γ-point of the Brillouin zone. Van Hove singularities emerge near the K-point, contributing step-like features to the density of states, while dominant optical peaks originate from band nesting at non-symmetric points.

Notably, the band nesting effect enables TMDs to achieve optical conductivities of approximately 1 mS, substantially

exceeding graphene's characteristic value of 0.06 mS.[45,46] Compared to the absorption signatures of A and B excitons near the band edges, C excitons exhibit exceptionally broad and intense absorption bands in high-energy nesting regions (Fig. 1(d)), underscoring their potential for designing advanced light-harvesting devices.[47] This unique combination of enhanced optical response and quantum-engineered electronic states positions high-energy excitons as key enablers for next-generation optoelectronic technologies.

2.2. Nonlinear optical response

The pronounced quantum confinement effects in the vertical dimension and the substantial exciton binding energies in 2D TMDs, as exemplified by monolayer MoS_2 and WS_2, give rise to complex excitonic many-body effects. This interplay between nonlinear optical phenomena and excitonic effects has significant implications for the design of nanoscale optoelectronic properties in contemporary 2D TMD systems. The resonant wavelength dependence of second harmonic generation (SHG) enables precise control of quantum excitonic behaviors in nanomaterials, facilitating efficient and tunable nonlinear optical responses.[48,49] Previous studies have extensively investigated the nonlinear optical phenomena associated with A and B excitons arising from valence band splitting. Notably, when the frequency-doubling energy in WSe_2 resonates with A and B excitons at cryogenic temperatures, the SHG signal exhibits a three-order-of-magnitude enhancement.[50] In molybdenum selenide-sulfide alloys, an increased selenium composition enhances the SHG intensity of B excitons relative to A excitons. This efficient modulation of nonlinear optical responses arises from the intricate coupling between exciton resonance broadening and defect state engineering.[51] These findings underscore the critical role of excitonic interactions in engineering quantum-enhanced optical functionalities for advanced nanophotonic applications.

High-energy C excitons come from band-nesting areas with intersecting energy bands, which leads to more intricate excitation processes and optical properties than band-edge A and B excitons. This multi-component nature endows C excitons with distinctive spectral signatures in absorption profiles and intricate energy-level structures, providing rich information for investigating nonlinear optical phenomena. Recent studies have explored C exciton-mediated nonlinear responses through various experimental approaches. One prominent strategy leverages the localized field enhancement from surface plasmon polaritons (SPPs). By combining monolayer WS_2 with subwavelength silver nano-groove gratings, Shi *et al.* showed effective coupling of C exciton resonances, significantly enhancing C exciton-driven nonlinear responses.[52] Figure 2(a) presents the reflection spectra of WS_2 on silver substrates, demonstrating redshifted plasmonic resonances that overlap with C exciton transitions in the grating-incorporated structure. Finite-difference time-domain (FDTD) simulations in Fig. 2(b) reveal strong in-plane electric field confinement along the Ag grooves, where the SHG wavelength (430 nm) associated with high-energy C excitons coincides with plasmonic resonances, thereby facilitating synergistic exciton–plasmon interactions. The SHG intensity exhibits dual resonance peaks near C exciton transitions (Fig. 2(c)), highlighting the high-resolution spectroscopic advantages of nonlinear processes. Remarkably, as shown in Fig. 2(d), the grating-patterned WS_2 regions achieve an SHG enhancement factor exceeding 400× compared to unpatterned areas, with a conversion efficiency reaching 2.0×10^{-5}, enabled by spectral matching between plasmonic modes and C exciton resonances.

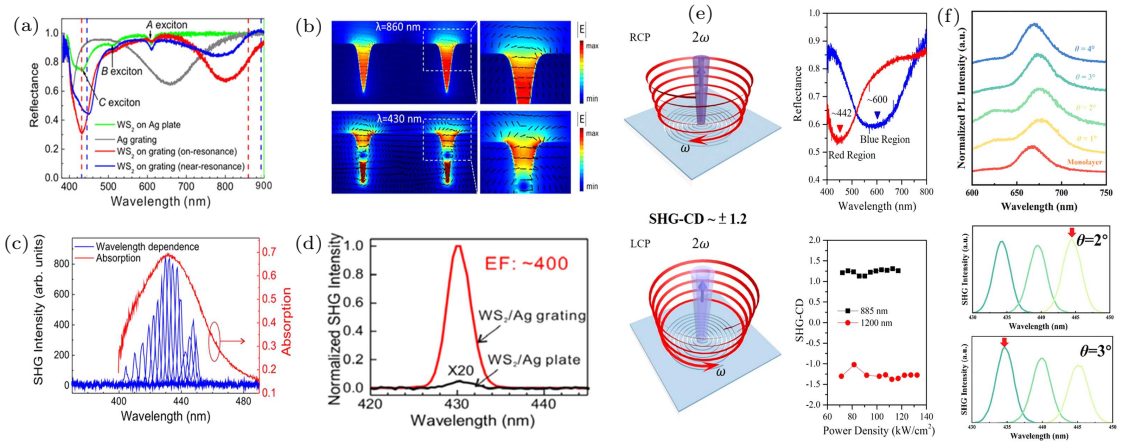


Fig. 2. (a) Reflection spectra of monolayer WS_2 on Ag substrates, demonstrating plasmon–exciton coupling in grating-incorporated structures.[52] (b) Finite-difference time-domain (FDTD) simulations of electric field distributions at fundamental (808 nm) and second-harmonic (404 nm) wavelengths.[52] (c) The dependence of the SHG intensity in the grating on the pump laser wavelength ranging from 810 nm to 900 nm, as well as the corresponding absorption spectra.[52] (d) The intensity ratio of the same WS_2 flake between the Ag grating and Ag plate regions reaches an SHG enhancement factor of 400.[52] (e) The geometric schematic diagram of aluminum plasma vortex lens. Reflection spectra from different measurement regions. The SHG circular dichroism at the C exciton resonance is ±1.2.[53] (f) SHG spectral shifts (445–435 nm) in twisted bilayer MoS_2 under C-exciton excitation, reflecting twist-angle-dependent band nesting modifications. The SHG spectra at small angles of 2° and 3°.[54]

Furthermore, although C excitons inherently lack valley-dependent chiral optical properties, Guo *et al.* engineered artificial chiral plasmonic structures (aluminum spiral metalenses) to induce spin-selective nonlinear responses.[53] As shown in Fig. 2(e), the reflection spectrum exhibits dual resonance peaks at 442 nm (tailored to WS_2 C excitons) and 600 nm. Through optical spin–orbit interactions, the bare aluminum spiral lens demonstrates exceptional SHG circular dichroism ($\pm 120\%$) at the C exciton resonance wavelength. This breakthrough establishes a novel approach for imparting chiral functionalities to originally achiral high-energy excitonic systems, thereby expanding their potential applications in spin-photonic devices and quantum information processing architectures.

The nonlinear optical response of C excitons can be further modulated by small twisting angles, a phenomenon associated with lattice reconstruction that alters band-nesting spacing and symmetry. The SHG technique can serve as a non-destructive method for characterizing the lattice reconstruction state of distorted bilayer MoS_2 by monitoring changes in the C exciton resonance.[54] As shown in Fig. 2(f), SHG spectra under C-exciton resonant excitation (800–980 nm) exhibit pronounced intensity variations correlated with twist angles. The SHG peak progressively blueshifts from 445 nm ($\theta = 2^\circ$) to 435 nm ($\theta = 3^\circ$), mirroring the corresponding C-exciton peak shifts in absorption spectra. This spectral alignment confirms band-nesting modifications induced by twist-angle-dependent lattice reconstructions, establishing SHG as a sensitive diagnostic tool for mapping atomic-scale structural transformations in twisted 2D heterostructures.

2.3. The exciton dynamics of high-energy excitons

The 2D TMDs have emerged as ideal materials for investigation of excitonic ultrafast dynamics due to their strong quantum confinement effects, high exciton binding energies (reaching hundreds of meV), and significant many-body interactions. Extensive research on excitonic dynamics has demonstrated their potential applications in optoelectronics, which is instrumental in designing high-performance nanophotonic devices. However, the photoluminescence (PL) quantum efficiency of the excitonic peaks is decreased from monolayers to multilayers due to the layer-dependent bandgap change in TMDs. Additionally, substantial differences in light absorption and carrier decay between high-energy and low-energy excitons have been observed, making exciton dynamics in TMDs a complex process. High-resolution femtosecond transient absorption (TA) spectroscopy can effectively capture the formation, thermalization, decay, and annihilation of these excitons on ultrafast timescales. Studying the ultrafast dynamics of high-energy excitons enables the differentiation and correlation of dynamical characteristics between low-energy excitons, thereby providing a microscopic understanding of carrier behavior variations among different excitonic states. Consequently, further investigation of the relationships between multiple exciton carrier dynamics and changes in high-energy exciton dynamics is essential.

2.3.1. The dynamics between high-energy excitons and band-edge A, B excitons

The interplay between crystal field effects and spin–orbit coupling in 2D TMDs promotes the formation of distinct multiparticle excitonic states. These interactions lift the degeneracy of energy levels in the valence band. Low-energy, strongly bound A and B excitons emerge as a result. Electronic transitions from the valence to conduction bands drive their formation. Energy and momentum conservations govern these transitions. Previous studies have systematically investigated carrier dynamics in low-energy excitonic systems. Manca *et al.* demonstrated a novel upconversion excitation mechanism in monolayer WSe_2, where resonant A-exciton excitation facilitates efficient B-exciton generation via interactions between two A excitons. The resulting high-energy electron–hole pairs subsequently relax into B excitons or 2s states of A excitons. This process revealed valley-selective exciton scattering dynamics and anomalous negative polarization emission, attributed to preferential intravalley B-to-A exciton scattering within the same momentum valley.[55] Complementary investigations by Plechinger *et al.* on WS_2 monolayers uncovered marked differences in spin-valley dynamics between A and B excitons, originating from conduction band spin splitting characteristics.[56] While A and B excitons exhibit high PL quantum yields at the K/K' valleys, C excitons display fundamentally distinct relaxation pathways. The parallel band alignment in C excitons induces spontaneous electron–hole separation and intraband relaxation, rendering them optically inactive. This contrasts sharply with the radiative recombination processes dominating A and B excitons' dynamics. Consequently, establishing connections between high-energy C-exciton dynamics and low-energy (A/B) excitonic behaviors is imperative for elucidating carrier interaction mechanisms. Further exploration of these inter-excitonic relationships will advance the understanding of quantum many-body effects and enable precise engineering of exciton-mediated optoelectronic functionalities in 2D TMDs systems.

Shi *et al.* employed broadband femtosecond transient absorption spectroscopy (FTAS) to elucidate the coupled dynamics and momentum-space delocalization characteristics of A, B, and C excitons in chemical vapor deposition (CVD)-grown monolayer MoS_2. Their work revealed that C excitons interact with A/B excitons through momentum-space coupling, with carrier relaxation dominated by defect scattering and phonon interactions.[57] Camellini *et al.* demonstrated anisotropic spectral blueshifts and distinct dynamic relaxation

rates of C and D excitons in nanostructured rippled MoS_2 under polarization perpendicular to the ripple axis. This phenomenon arises from shape anisotropy-induced modifications in electron–phonon coupling, which further modulate the ultrafast dynamics of C excitons.[58] Kozawa *et al.* systematically investigated band nesting-mediated regulation of photocarrier dynamics in 2D TMDs, as illustrated in Fig. 3(a).[59] In MoS_2 systems, when excitation energy resonates with band-nesting regions, electrons relax to the Λ valley of the conduction band while holes migrate to the Γ peak of the valence band. Notably, the relaxation pathways of photocarriers in C excitons differ significantly between monolayers and bilayers. Monolayer systems exhibit suppressed photoluminescence excitation (PLE) intensity under C-exciton excitation, indicating reduced A-exciton recombination due to momentum-space separation of photocarriers. Conversely, bilayer configurations show enhanced indirect PLE peaks with weaker direct emission (A-peak) enhancement, confirming that band nesting promotes indirect excitonic transitions. Schematic diagrams elucidate photocarrier relaxation trajectories under C-exciton excitation, highlighting layer-number-controlled directional manipulation of carrier relaxation pathways. TA spectroscopy serves as a powerful tool for probing ultrafast carrier dynamics between high-energy and band-edge excitons. Our group's previous work revealed a bidirectional coupling mechanism between C excitons and band-edge A excitons in monolayer WS_2, as illustrated in Fig. 3(b).[60] High-energy pump excitation induces C-exciton relaxation through distinct fast and slow processes that temporally coincide with A-exciton decay dynamics. Under 515 nm excitation, thermalized carriers from C-exciton relaxation compensate for A-exciton losses via carrier–phonon scattering ($\sim$ 10 ps) and direct electron–hole recombination ($<$ 100 ps), effectively delaying A-exciton decay. Conversely, sub-C-exciton-energy excitation enables band-edge A excitons to upconvert into C excitons through multibody processes such as exciton–exciton annihilation (EEA) or defect-assisted Auger recombination. This bidirectional exciton coupling mechanism facilitates enhanced utilization of photoexcited carriers.

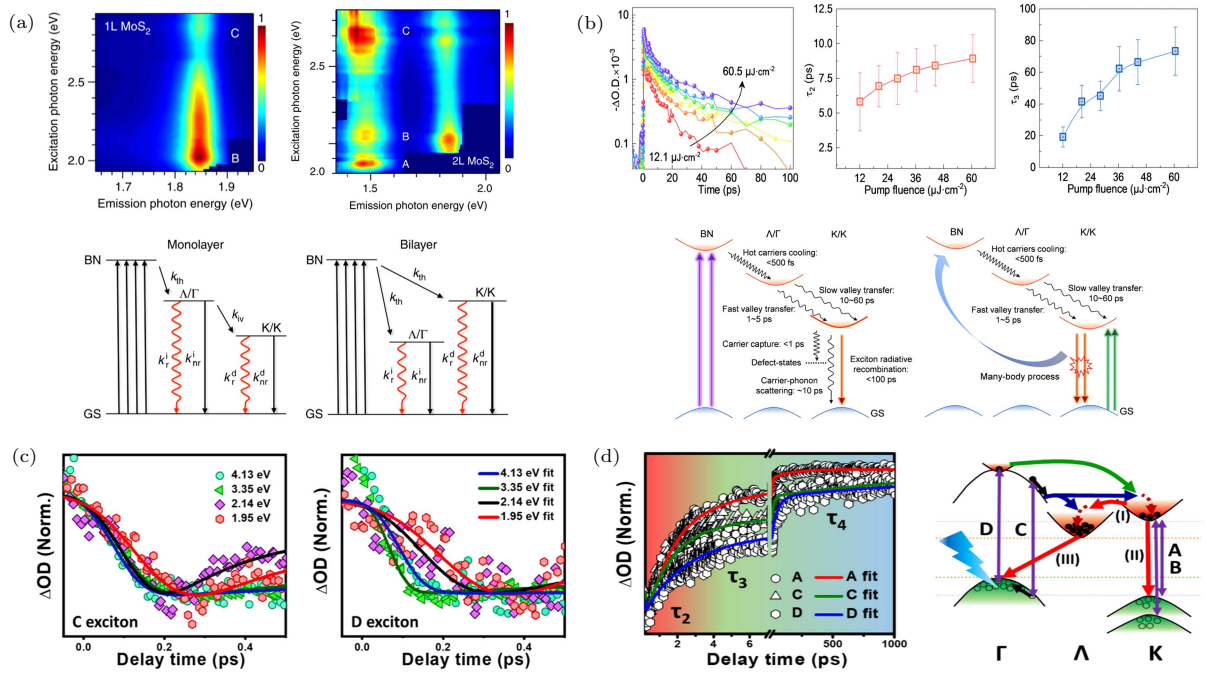


Fig. 3. (a) The PLE intensity map of bandgap emission for monolayer and bilayer MoS_2. Schematic illustration of the photogenerated carrier relaxation mechanism in monolayer and bilayer TMDs materials.[59] (b) The pump-fluence-dependent A-exciton dynamics in monolayer WS_2 under 515 nm excitation. τ_2 and τ_3 represent the intermediate and slow decay components, respectively.[60] (c) Transient dynamics of high-energy C/D excitons under different pump energies.[62] (d) Normalized relaxation trajectories of A, C, and D excitons after 3.35 eV photoexcitation, with schematics of intervalley scattering pathways.[62]

Beyond single layers, the interaction between high-energy C and D excitons and low-energy A and B excitons, as well as the regulation of exciton relaxation mechanisms in few-layer TMDs, is particularly significant. Borzada *et al.* reported the relaxation dynamics of A, B, and C excitons in few-layer MoS_2, which mainly encompass the generation, rapid dissociation, and decay processes of excitons.[61] Goswami *et al.* investigated the formation and relaxation processes of high-energy C/D excitons and low-energy A/B excitons in few-layer WS_2, systematically revealing the regulatory mechanisms of band nesting effects, intervalley scattering, and many-body processes on exciton relaxation.[62] As shown in Fig. 3(c), the formation time of C/D excitons can be rapidly achieved under high-energy pump excitation, whereas low-energy pumping can only induce the generation of C excitons through many-body processes, such as interband tunnel-

ing, with the ineffective generation of D excitons due to the lack of energy band overlap with the K valley. Figure 3(d) shows that the relaxation time of C/D excitons is significantly longer than that of A excitons, primarily attributed to the indirect recombination between the Λ valley and the K valley and the intervalley scattering processes. At high carrier densities, valley filling in the K valley and the Pauli blocking effect delay the intervalley transfer of C/D excitons.

2.3.2. The relaxation and extraction of hot carriers in high-energy excitons

Hot carriers, defined as high-energy charge carriers above the band edge, possess significant research value and application potential in various fields including photocatalysis, photovoltaic device design, photodetection, and high-speed electronic devices.[63–65] For example, due to their high reactivity, hot carriers can lower the effective potential barrier required for photocatalytic reactions, thereby facilitating and improving reaction efficiency. Furthermore, hot carriers not only increase the photoelectric conversion efficiency of photovoltaic devices but also broaden the spectral detection range, enhancing light energy collection and utilization. Consequently, the completion of the processes of hot carrier generation, relaxation, and extraction requires an in-depth study of the kinetic processes of hot carriers.

In 2D materials, hot carriers relax quickly to the band edge. This relaxation occurs on a sub-picosecond timescale. Two main factors cause this rapid relaxation: carrier–carrier scattering and thermal phonon effects. This fast thermalization process significantly hinders efficient hot carrier extraction. Therefore, slowing hot carrier cooling has become crucial for the practical applications of hot carriers. In energy band nesting regions, high-energy excitons exhibit spontaneous electron–hole separation, which also results in a substantial difference in the relaxation process of hot carriers within their energy bands compared to those at the band edge.

Wang and colleagues investigated the cooling behavior of hot carriers associated with C excitons in monolayer MoS_2.[66] A graphene heterostructure design was implemented to achieve efficient extraction of these hot carriers. As shown in Fig. 4(a), a global analysis of transient absorption spectroscopy on the MoS_2 monolayer yielded four lifetime components (0.27 ps, 1.3 ps, 23 ps, and 1.5 ns), with A and B excitons undergoing rapid decay, while the lifetime of C excitons was extended to 23 ps. This reflects the slow cooling characteristics of hot carriers associated with C excitons, which stem from the spontaneous electron–hole separation in the band nesting regions. In the MoS_2/graphene heterostructure, the TA spectrum revealed only three lifetime components, indicating rapid charge transfer to graphene (Fig. 4(b)). Graphene, through its dielectric screening effect, reduced the exciton binding energy (E_b) of MoS_2, promoted the vertical separation of photogenerated charges, and modulated the electronic structure of MoS_2, achieving an efficient extraction of 80% for the hot carriers associated with the C excitons.

The slow cooling of high-energy excitons is critical for achieving efficient hot carrier extraction. Therefore, identifying the origin of this slow cooling and analyzing and controlling its mechanisms are essential. Our team employed femtosecond transient absorption spectroscopy to demonstrate that the cooling mechanism of C excitons originates from intervalley transfer.[67] Figure 4(c) illustrates the relaxation dynamics of C excitons under low and high pump flux conditions to verify the Pauli blocking effect. At higher light intensities, exciton–exciton annihilation accelerates exciton recombination, weakening the Pauli blocking effect and significantly reducing the relaxation time of C excitons. However, the photobleaching signal of C excitons increases nonlinearly with increasing pump intensity, confirming the dominant role of intervalley transfer (Fig. 4(d)). By normalizing and comparing the decay signals of A excitons under different pump intensities (1.3 $\mu J \cdot cm^{-2}$ and 127 $\mu J \cdot cm^{-2}$), we identified a compensating signal under high pump intensities. The fitting results of the compensating signal decay curve matched the cooling time of C excitons, confirming that intervalley transfer dominates the slow cooling of C excitons. Additionally, Rose *et al.* coupled C excitons in few-layer MoS_2 with surface plasmon polaritons, utilizing their delocalization to suppress defects and intervalley scattering, thereby significantly extending the cooling time of C excitons.[68] This strong-coupling approach offers a new strategy for hot carrier extraction. Recently, Wei *et al.* used transient absorption microscopy (TAM) to reveal the anomalous negative diffusion of hot carriers in monolayer MoS_2, attributed to the spatially non-uniform hot phonon bottleneck (HPB) induced by Gaussian pump beams.[69] By enhancing the HPB effect through high pump flux, the lifetime of hot carriers was prolonged, providing a method to optimize hot carrier extraction efficiency.

D excitons, located on the high-energy side of C excitons as shoulder excitons, exhibit more complex structures along with higher kinetic energy and greater degrees of freedom. Investigation of their relaxation dynamics may enhance the application potential of high-energy excitons. Tran *et al.* demonstrated the advantages of the slow cooling mechanism of D excitons in monolayer MoS_2 and their potential applications in heterostructures.[70] Figure 4(e) illustrates the formation mechanism of D excitons. The slow rise of D excitons in TA spectra under low pump energy indicates intervalley carrier–carrier scattering from the K valley to the Γ valley. The pump-energy independence of D excitons suggests they are generated via an indirect process, supporting their free carrier characteristics. D excitons also exhibit slow cooling dy-

namics, significantly shower than those of C excitons and 2–3 orders of magnitude slower than conventional semiconductors such as perovskites and quantum dots. As shown in Fig. 4(f), the intervalley scattering from the Γ valley to the Λ and K valleys, along with the differences in electronic structure between high-energy and low-energy bands, contributes to this complex slow cooling mechanism. To investigate hot carrier extraction from D excitons, a type-II heterojunction can be formed between the Γ valley of MoS_2 and the conduction band of TiO_2. The built-in electric field facilitates electron transfer from MoS_2 to TiO_2. As depicted in Fig. 4(g), the prolonged cooling time of hot carriers in the Γ valley of D excitons allows more electrons to complete the transfer. The combination of free carrier characteristics and slow cooling results in substantially higher hot carrier extraction efficiency for D excitons (98%) compared to C excitons (87%). This dual mechanism — intervalley scattering delaying high-energy exciton cooling and interfacial charge separation in heterojunctions — enhances hot carrier extraction efficiency, presenting a promising strategy for the design and utilization of hot carrier-based devices.

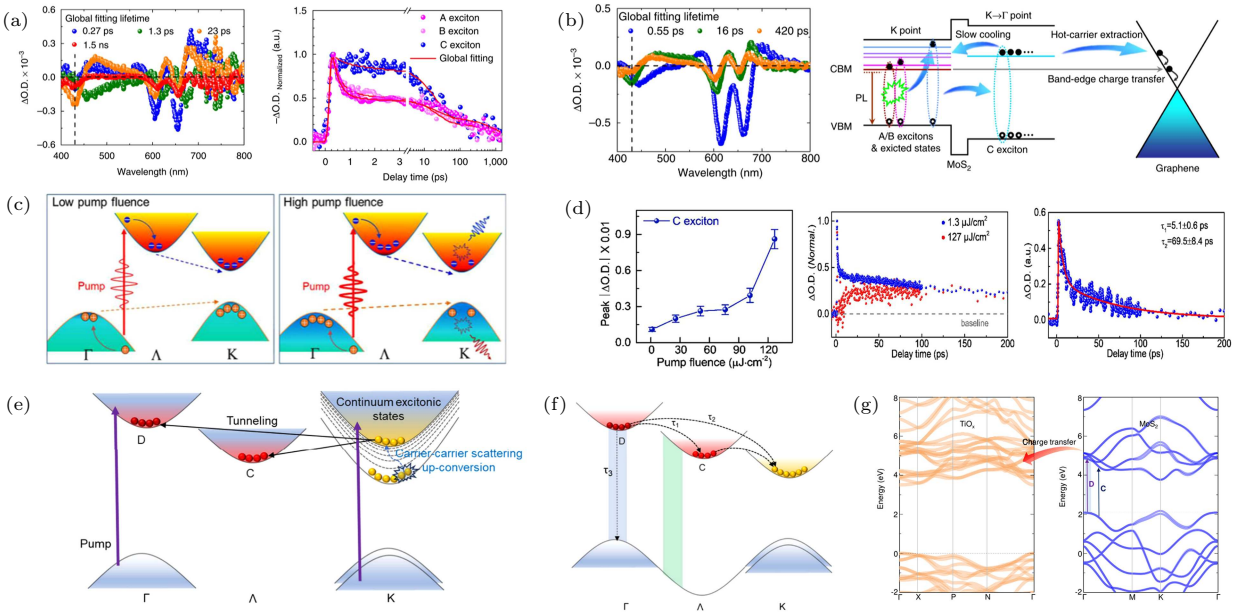


Fig. 4. (a) Under 400 nm excitation, the global analysis results of transient absorption spectroscopy for monolayer MoS_2. The normalized decay kinetics of A, B, and C excitons under the same pump condition.[66] (b) Schematic diagrams of the normalized attenuation kinetics of A, B and C excitons in monolayer MoS_2 under a pump condition of 400 nm and the charge transfer process in the corresponding graphene heterostructure.[66] (c) Schematic illustration of the photophysical processes excited by low and high pump fluences in monolayer MoS_2.[67] (d) The function related to the peak energy of C exciton with respect to pump fluence. The decay kinetics and fitting curves of two different pump fluence intervals for A exciton.[67] (e) Schematic diagram illustrating the generation mechanism of D excitons through intra-K-valley scattering and Γ-valley tunneling.[70] (f) The slow scattering path from the Γ point to the Λ/K point in D excitons.[70] (g) Schematic illustration of the energy band structure and hot carrier transfer between monolayer MoS_2 and TiO_x.[70]

2.3.3. Defect state-mediated localization of high-energy excitons

In large-area monolayer TMDs synthesized via chemical vapor deposition (CVD), sulfur and selenium vacancies are unavoidable. Consequently, investigating exciton localization and ultrafast dynamics in defect states becomes essential. Substantial advancements have been achieved in single-photon emission, energy transfer, exciton transport, and the regulation of spin and valley degrees of freedom in TMDs through the study of interactions between defect states and exciton effects.[71–73] Zhang *et al.* found that increased defect state density accelerates the EEA rate and reduces luminescence efficiency.[74] Liu *et al.* visualized the interaction between defects and exciton transport dynamics in 2D TMDs using TAM spatially and temporally resolved measurements.[75] Elucidating the ultrafast dynamics between defect states and high-energy exciton relaxation is pivotal for advancing the manipulation and applications of high-energy excitons in 2D TMDs.

Qu *et al.* revealed defect-mediated localization of high-energy excitons and their relaxation behavior using fs-TA spectroscopy.[76] As illustrated in Fig. 5(a), under 515 nm excitation, electrons from C excitons become trapped in defect energy levels while holes remain in the valence band, forming localized C excitons. This defect-mediated direct excitation process, which remains unaffected by pump fluence, differs from the band transition mechanism responsible for free C exciton formation. Distinct differences emerge in TA spectra when comparing C exciton excitation under 343 nm and 515 nm pumping: the C exciton peak exhibits a blueshift (redshift) under low-energy (high-energy) excitation. The blueshift of localized C exciton peaks in Fig. 5(b) results from hole tilting from the Λ to Γ points in the valence band, which increases the bandgap of localized C excitons. Conversely, the

redshift of free C excitons primarily stems from band renormalization, where band tilting effects are counterbalanced by simultaneous hole–electron diffusion. The relaxation pathway of localized C excitons involves both intraband and intervalley transfer. Sulfur vacancies localize C excitons, thereby restricting electron and hole relaxation and prolonging intervalley transfer times. Simultaneously, phonon-assisted hole intraband scattering enhances the intraband transfer rate of C excitons, highlighting the potential of defect engineering for optimizing optoelectronic device design.

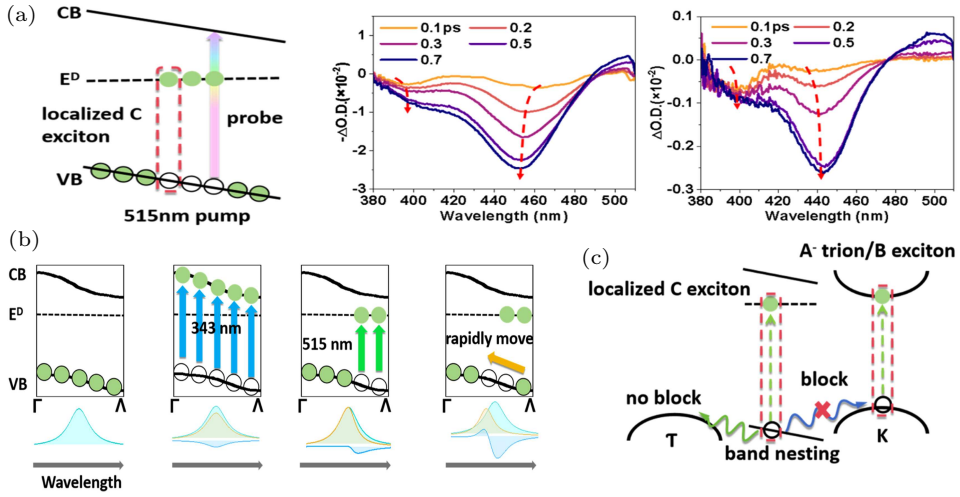


Fig. 5. (a) The defect-mediated direct excitation model of C excitons. The peak positions of high-energy C excitons and D excitons vary with delay time under 515 nm and 343 nm pumping.[76] (b) The electron–hole distribution of C excitons and the variation in absorption spectra under different pumping conditions.[76] (c) The relaxation pathways of localized C excitons, including intraband (represented by light green arrows) and inter-valley (represented by blue arrows) transfers.[76]

2.4. The resonance effect of high-energy excitons

The significant light–matter interactions in 2D TMDs arise from quantum confinement and weakly screened excitons with high binding energies, resulting in excitonic resonances at specific wavelengths that manifest as distinct spectral peaks. These resonances provide unique advantages for enhancing Raman scattering, activating interlayer vibrational modes, and manipulating phonon states through tailored light–matter interactions.[77–79]

Raman spectroscopy serves as a powerful tool for investigating the stacking, layer coupling, and strain in 2D TMDs. When excitation energies align with excitonic transitions, resonance effects can significantly enhance specific Raman signals. Lee *et al.* demonstrated that in few-layer MoS_2, C-exciton resonance selectively amplifies interlayer breathing modes, with peak positions sensitive to stacking configurations (2H, 3R, mixed), whereas high-frequency E_g and A_g modes exhibit no phase dependence.[80] Kim *et al.* showed that in few-layer $MoSe_2$, C-exciton resonance modulates both interlayer shear and breathing vibrations (Fig. 6(a)), unlike A-exciton resonance, which obscures low-frequency modes.[81] McCreary *et al.* observed a 50 meV shift in C-exciton resonance peaks between 2H- and 3R-stacked WSe_2 bilayers, confirming stacking-dependent energy modulation.[82] First-principles calculations by Wang *et al.* revealed that in monolayer MoS_2, C-excitons enhance Raman scattering through energy accumulation in excitonic states and wavefunction rehybridization, accounting for the absence of A/B-exciton resonance responses.[83] While A/B excitons couple to intralayer phonons (K-point), high-energy C-excitons at the Γ-point exhibit strong interlayer vibrational coupling, with layer-dependent signal enhancement.[84]

Bilgin *et al.* combined experiments and theoretical calculations to investigate the double resonance Raman processes and phonon coupling mechanisms of C excitons in high-quality $MoSe_2$ single crystals.[85] As shown in Fig. 6(b), the intensity ratios of the A_1'/E' and $2ZA/E'$ peaks both exhibit maxima near 2.54 eV (488 nm), corresponding to the C exciton energy. High-energy C exciton resonance enhances electron-phonon scattering dominated by the A_1' and $2ZA$ phonon modes. To confirm the origin of the Raman peaks, double resonance Raman simulations demonstrated a prominent double resonance peak at 250 cm^{-1} under 488 nm excitation, consistent with the experimental $2ZA$ mode (Fig. 6(c)), confirming the correlation between ZA phonons and C exciton resonance. The 2.54 eV isoenergetic contour in the Brillouin zone revealed a double resonance path with momentum matching between electrons and ZA phonons. From the band structure perspective, high-energy electrons excited to the conduction band are scattered back via ZA (M-point) phonons, forming a double resonance process. The combination of experimental and theoretical results revealed the phonon double resonance characteristics under C exciton energy matching. This double resonance mechanism based on C exciton resonance can also activate forbidden phonon modes associated with intrinsic defects in monolayer and few-layer MoS_2, with Raman

peak frequencies showing significant layer-dependent variations, highlighting the sensitivity of phonon modes to layer number under C exciton resonance.[86] Trovatello *et al.* used Fourier-transform (FT) spectroscopy at different pump energies to probe coherent phonon oscillations at the C exciton peak position.[87] As shown in Fig. 6(d), when the pump energy approaches the C exciton resonance energy (2.95 eV), the amplitude of the A_1^- phonon mode (406 cm^{-1}) is significantly enhanced, reaching a maximum, and decreases sharply when the pump energy deviates from the C exciton energy, indicating a strong correlation between A_1^- phonons and C exciton resonance. The theoretically calculated Raman tensor peak positions showed resonance enhancement consistent with experimental results, confirming that C exciton resonance can efficiently modulate A_1^- phonon coherence and demonstrating a strong coupling mechanism between C excitons and A_1^- phonons.

In bilayer TMDs, the interlayer twist angle influences the symmetry of interlayer atomic arrangements, generating a distinctive moiré superlattice effect and tunable interlayer coupling properties. Schneider *et al.* proposed a method to detect the interlayer coupling strength in bilayer TMDs by using optically excited interlayer Raman modes under C-exciton resonance.[88] As shown in Fig. 6(e), under C-exciton energy resonance excitation (514 nm), interlayer E_g and A_g Raman peaks appear distinctly at different angles. Comparative analysis of Raman spectra for MoS_2 and $MoSe_2$ at different excitation wavelengths confirmed the correlation between C-exciton resonance excitation and the intensity of interlayer modes. These findings demonstrate that the detection of interlayer coupling states in twisted bilayer TMDs through C-exciton resonance represents a highly efficient approach.

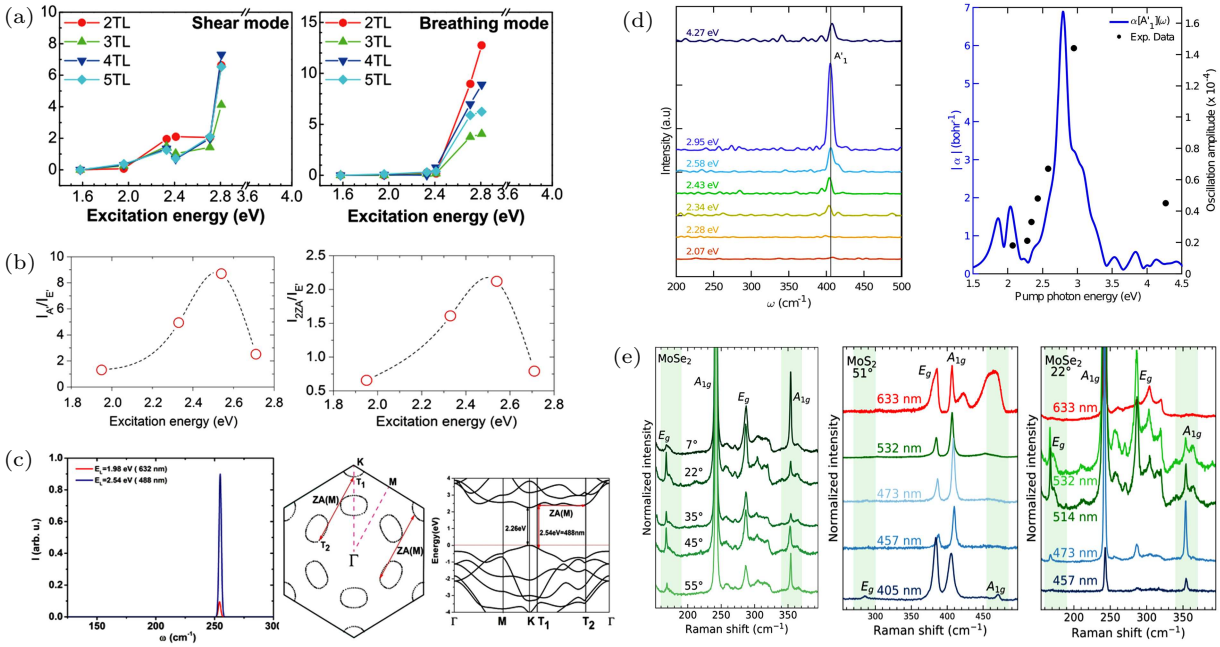


Fig. 6. (a) The Raman intensity contour of 2TL to 5TL $MoSe_2$ varies with different excitation energies.[81] (b) The Raman intensity ratios of the A' peak and the $2ZA$ peak to the E' peak under different excitation energies, respectively.[85] (c) Simulation of double-resonance Raman intensity under two excitation wavelengths (632 nm and 488 nm). The isoenergetic contour map under 2.54 eV excitation in the Brillouin zone of monolayer $MoSe_2$, as well as the double-resonance process scattered by $ZA(M)$ phonons during electron transitions in the electronic band structure.[85] (d) Fourier transform (FT) spectra of monolayer MoS_2 under varying pump energies. Comparison of the measured A_1^- phonon amplitude (normalized values) with theoretical values derived from Raman tensor analysis.[87] (e) Raman spectra of twisted bilayer $MoSe_2$ under C exciton resonance energy excitation. Comparison of Raman spectra of MoS_2 and $MoSe_2$ under different excitation wavelengths.[88]

3. Advances in application research based on the characteristics of high-energy excitons in 2D TMDs

As mentioned in Subsection 2.4, the complex resonance phenomenon of high-energy excitons not only provides profound insights into the dynamic interaction between electronic states and vibrational dynamics, but also establishes a fundamental framework for longitudinal light–matter interactions at the quantum level. The synergy between this fundamental characteristic and the engineering of applied devices serves as a reference for the breakthroughs in ultraviolet-enhanced luminescence discussed in Subsection 3.1. In this section, material integration and energy funnel mechanisms are employed to address the inherent limitations of high-energy exciton utilization. In the realm of low-dimensional semiconductors, the pronounced light–matter interactions in 2D TMDs have emerged as a cutting-edge research focus for optical property engineering and optoelectronic device design. This phenomenon is intrinsically linked to the robust excitonic effects arising from quantum confinement and reduced dielectric screening in TMDs. Notably, band-nested regions in the

Brillouin zone (the C-exciton region), characterized by parallel energy alignment of conduction and valence bands, contribute to strong ultraviolet absorption in optical spectra, corresponding to the enhanced density of states near Van Hove singularities. These unique high-energy states hold significant potential for broadening the spectral response range of photodetectors and improving light emission efficiency and photoelectric conversion performance. However, the practical application of high-energy excitons is impeded by substantial challenges arising from competing relaxation mechanisms — rapid intravalley nonradiative recombination and inefficient intervalley transfer of hot carriers. These limitations impose stringent constraints on the design and performance of devices in relevant technological contexts. Consequently, developing novel experimental strategies to enhance the utilization efficiency of high-energy excitons is critical for advancing ultraviolet optoelectronic devices based on TMDs. In the following sections, we discuss potential application directions and device design concepts leveraging high-energy excitons, focusing on three key aspects: ultraviolet photoelectric conversion systems, light-emission efficiency enhancement, and strain-sensing probes. Optimizing performance and engineering devices based on high-energy excitonic properties will significantly expand the functional applications of TMDs materials.

3.1. Improvement of photoluminescence efficiency based on high-energy excitons under ultraviolet excitation

High-energy excitons exhibit pronounced and broad ultraviolet (UV) absorption characteristics due to their band-nested structure with parallel band alignment. However, under C-exciton resonance excitation, the photogenerated carriers struggle to relax effectively to the band edges for radiative recombination. Notably, unlike the direct radiative recombination within the *K* valley for band-edge excitons, the electrons and holes in C-excitons predominantly undergo nonradiative recombination processes, involving rapid intravalley relaxation and slow inter-valley scattering. The photoluminescence efficiency of TMDs materials excited in the UV range is significantly suppressed compared to that excited in the visible light range. Therefore, constructing new channels for the utilization of light energy targeting the relaxation processes of C-excitons is crucial for enhancing photoluminescence efficiency.

Yan *et al.* constructed a novel rare-earth-doped $LaPO_4$:Tb^{3+}/WS_2 hybrid system to investigate Förster resonance energy transfer (FRET)-mediated enhancement of PL efficiency in TMDs.[89] As shown in Fig. 7(a), the fluorescence microscopy images of monolayer WS_2 reveal suppressed PL intensity with increasing excitation energy, particularly in the UV spectral region, reflecting the inhibitory effect of band nesting on radiative recombination under high-energy excitation. To circumvent this limitation, a strategic design was implemented by creating alternative energy transfer channels that bypass band-nested regions, thereby directly enhancing direct bandgap radiative recombination in WS_2. Figure 7(b) illustrates the hybrid system architecture, where Tb^{3+}-doped $LaPO_4$ nanorods are directly integrated with monolayer WS_2 to establish UV-driven energy transfer pathways. Unlike conventional UV excitation generating C-excitons, Tb^{3+} ions in the hybrid system absorb UV photons and transfer energy non-radiatively to the WS_2 monolayer via resonant coupling. Remarkably, as demonstrated in Figs. 7(c) and 7(d), the hybrid structure exhibits a tenfold PL enhancement under 325 nm excitation. This improvement originates from Tb^{3+}-mediated downconversion of high-energy UV excitation to lower-energy excited states ($^5D_4$ level), enabling resonant energy transfer to WS_2 band-edge free excitons. This mechanism effectively suppresses direct C-exciton generation while demonstrating the superior efficiency of FRET in boosting luminescence yield. Notably, this strategy exhibits generalizability across other TMDs materials, with the nanorods concurrently providing protective effects on TMDs layers.

In contrast to strategies that introduce new absorption/emission centers for energy transfer within hybrid systems, constructing type-I heterojunctions to enable rapid interfacial charge transfer represents an alternative high-efficiency energy utilization approach. Designing a dual type-I cascaded channel between C-excitons and band-edge excitons has been demonstrated as an effective method to enhance hot carrier utilization from C-excitons.[90] As illustrated in Fig. 7(e), the heterostructure comprising monolayer WS_2 and CdS quantum dots facilitates both rapid hot carrier transfer from C-excitons to CdS and subsequent carrier recycling back to the WS_2 band edge to form A-excitons. This "round-trip" carrier pathway effectively circumvents the intrinsic nonradiative recombination channels of C-excitons. Figure 7(f) demonstrates that the PL intensity of WS_2 in the heterostructure is significantly amplified, while that of CdS is suppressed, yielding a heterostructure photoluminescence quantum yield (PLQY) of 11.1%, indicative of efficient charge transfer. Spatially resolved PL intensity mapping further corroborates this enhancement, ensuring experimental reproducibility. Transient absorption spectroscopy directly monitors carrier dynamics through time-resolved excited-state absorption (ESA) and ground-state bleaching (GSB) signals, elucidating microscopic charge transport mechanisms. As shown in Fig. 7(g), the heterostructure exhibits weakened C-exciton bleaching signals and intensified A-exciton bleaching signals. Kinetic analysis reveals a reduction in C-exciton lifetime from 53 ps to 27 ps, accompanied by a prolongation of A-exciton lifetime from 54 ps to 108 ps, achieving a charge transfer efficiency of 50%. This efficient hot carrier transfer mechanism substantially enhances the UV-excited PL quantum yield in TMDs, serving as a successful paradigm for engineering exciton dynamics in 2D materials.

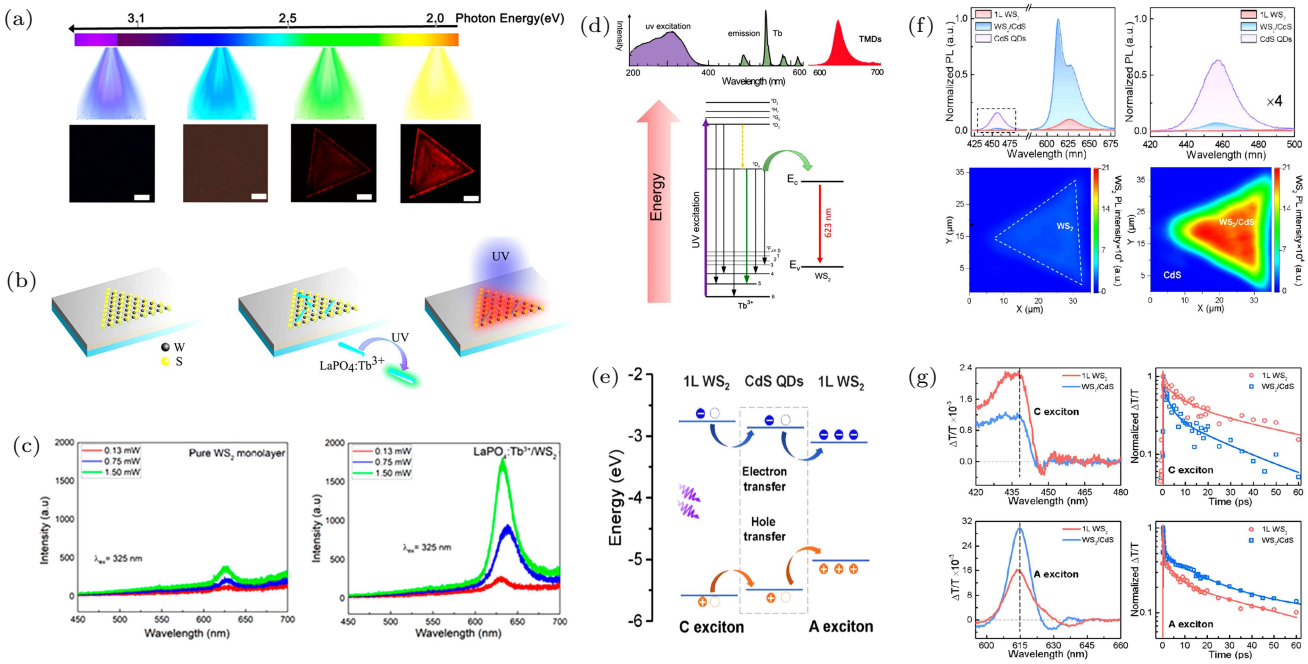


Fig. 7. (a) Fluorescence microscope images of monolayer WS_2 under different excitation wavelengths.[89] (b) Schematic diagram of the $LaPO_4$:Tb^{3+}/WS_2 hybrid structure design and the FRET energy transfer pathway.[89] (c) Comparison of PL spectra of individual WS_2 and hybrid structures under ultraviolet excitation.[89] (d) Schematic illustration of the energy transfer process in the hybrid structure under ultraviolet excitation.[89] (e) Schematic illustration of energy band alignment and carrier transfer pathways in heterostructures.[90] (f) PL intensity variation and PL intensity mapping of individual WS_2, CdS quantum dots, and heterojunctions under 405 nm excitation.[90] (g) TA spectral variation diagrams of C exciton and A exciton in individual WS_2 and heterojunctions, respectively. The right figure is a comparison chart of exciton decay kinetics.[90]

3.2. Optoelectronic devices based on high-energy excitons

Photonic devices, which utilize the photoelectric effect to achieve mutual conversion between optical and electrical signals, have been extensively investigated for applications in photodetection, optical communication, and bio-inspired vision systems.[34,36,91–93] Compared to conventional semiconductors, 2D TMDs exhibit superior optoelectronic characteristics, including high optical absorption coefficients spanning from visible to near-infrared wavelengths, layer-dependent tunability of band structures, and exceptional carrier mobility. The direct bandgap in monolayer TMDs generates robust excitonic effects under photoexcitation, enabling efficient generation of electron–hole pairs and supporting stable exciton manipulation at room temperature — properties that meet the requirements of high-sensitivity optoelectronic applications. These excitonic effects enhance light absorption and emission processes, while the unique band-nested architecture in 2D TMDs facilitates strong coupling between high-energy excitons and high-photon-energy UV radiation. This synergy not only improves UV spectral absorption but also enhances device performance metrics such as response speed and detection sensitivity, thereby advancing the efficiency of next-generation optoelectronic systems.

In visual systems, 2D TMDs-based optoelectronic synaptic devices integrate multifunctional properties to emulate visual perception while simultaneously simulating wavelength-dependent nociception in response to harmful light stimuli. Recently, our research group developed a monolayer MoS_2-based optoelectronic synaptic device by combining the high-energy C-exciton band nesting effect with defect-induced charge trapping mechanisms.[94] This device demonstrates biomimetic pain responses to optical stimuli, as shown in Fig. 8(a). By applying simultaneous dual-light-pulse stimulation using green and UV light, the total current reached 87 pA, with the UV response exhibiting slow decay and sustained activity, resulting in an asymmetric variation curve (Fig. 8(b)). For this device, UV light input (short-wavelength) delays the carrier trapping process, resulting in a larger time constant. Figure 8(c) compares the photocurrent responses under long- and short-wavelength excitation, showing that the photocurrent intensity exhibits a superposition effect at different time intervals. The significantly stronger UV photocurrent amplitude arises from the high-energy exciton band nesting effect, which enhances short-wavelength absorption efficiency, thereby increasing the number of photogenerated carriers and amplifying the current response. This confirms the device's sensitivity in simulating UV-induced pain perception. The temporal regulation of light signals is crucial for spatiotemporal encoding in neuromorphic computing. As shown in Fig. 8(d), combinations of 532 nm and 320 nm light inputs enable multiple optical logic functions. AND logic is achieved when both light pulses are applied simultaneously with a pulse width of 5 s, producing an output current exceeding the threshold of 154 pA. OR logic can be realized with a single light pulse input of 25 s pulse width to trigger the threshold current. NAND/NOR logic is implemented by inverting the "on"

and "off" states of the light signals, enabling complementary operations. This flexible photonic logic not only achieves all-optical logic functionality but also simplifies the design complexity of traditional optoelectronic hybrid devices.

Self-powered ultraviolet photodetectors can directly convert UV light energy into electricity without external power, featuring low power consumption and high sensitivity, making them a key research focus in recent years. Although TMDs materials have high UV light absorption coefficients and charge transfer rates, their bandgap is limited to the visible to near-infrared range, hindering direct UV detection. Previously, the construction of heterojunctions with wide-bandgap semiconductors served as an effective strategy to enhance the performance of self-powered devices. This approach not only preserves the high UV response from the wide bandgap but also accelerates exciton separation via the built-in electric field at the interface, boosting photocurrent and response speed, as seen in combinations like MoS_2/β-Ga_2O_3,[95] $PtSe_2$/GaAs,[96] and WS_2/GaN.[97] Recently, Wang *et al.* achieved 92% external quantum efficiency (EQE) and 270 mA·W^{-1} responsivity under 365 nm illumination in WS_2.[98] This high carrier separation efficiency stems from defect-free van der Waals (vdW) metal contacts and optimized channel structures. However, the rapid recombination relaxation mode of high-energy exciton charges under UV illumination still severely limits carrier transfer and utilization efficiency in TMDs. To further optimize TMD-based photodetectors, it is essential to maintain the strong light absorption of high-energy excitons while simultaneously enhancing carrier transfer efficiency.

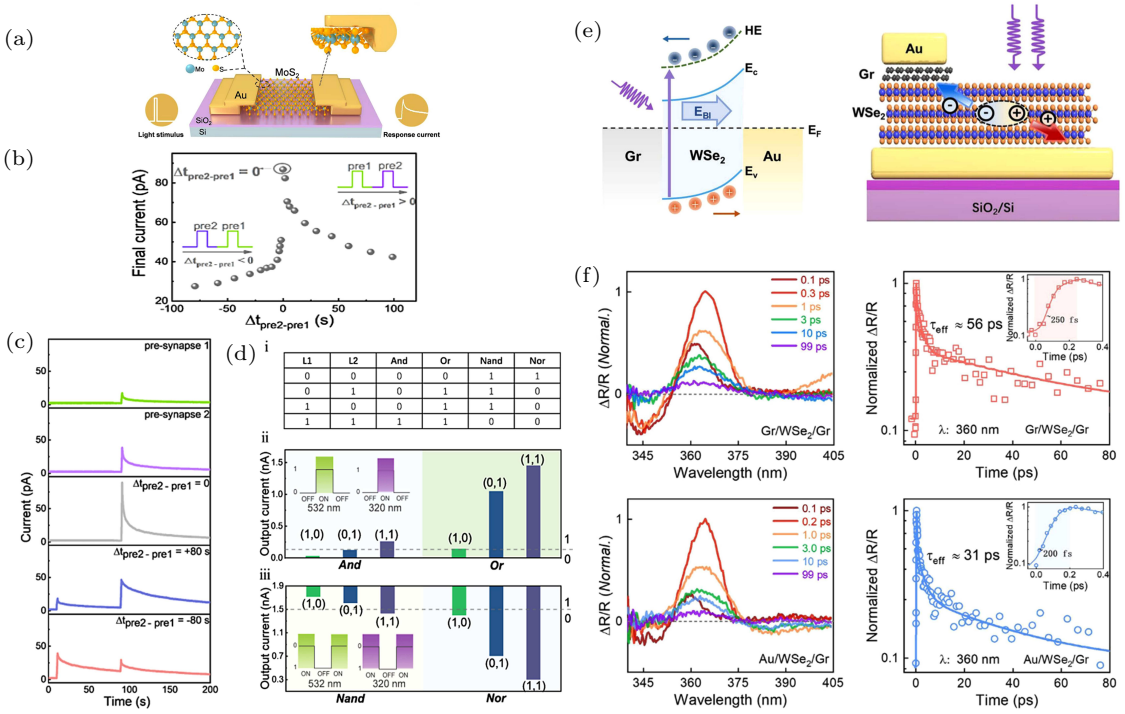


Fig. 8. (a) Optical synaptic device structure based on Van der Waals electrode-integrated monolayer MoS_2.[94] (b) Spatial and temporal summation decay curves of photocurrent under dual-wavelength optical input as a function of pulse interval.[94] (c) Photocurrent variation diagrams of synapse 1 and synapse 2 at different time intervals.[94] (d) Optical logic operation functions under various light pulse widths and intensity regulations.[94] (e) Working principle of the built-in electric field with energy band alignment and schematic diagram of the Au/WSe_2/Gr photodetector device structure.[99] (f) TA spectra and corresponding normalized decay curves of two types of Gr/WSe_2/Gr and Au/WSe_2/Gr photodetector devices under 300 nm pumping.[99]

Our group discovered that in multilayer WSe_2, a strong built-in electric field formed by a unilateral Schottky junction effectively suppresses C-exciton recombination, thereby promoting the separation and extraction of hot carriers.[99] As shown in Fig. 8(e), WSe_2 forms a unilateral Schottky contact with the bottom Au electrode and a quasi-Ohmic contact with the top graphene electrode. The Schottky barrier (hole) at the interface causes upward band bending, driving high-energy electrons to rapidly transfer toward the graphene electrode under the strong built-in electric field, thereby reducing the probability of non-radiative recombination of C-excitons. By comparing the TA spectra of Gr/WSe_2/Gr and Au/WSe_2/Gr devices, we analyzed and fitted the decay dynamics of photogenerated carriers in the two devices (Fig. 8(f)). The exciton lifetime in the Au/WSe_2/Gr device was 31 ps, significantly shorter than that in the Gr/WSe_2/Gr device (56 ps), which lacked a built-in electric field to drive C-exciton separation. This clearly demonstrates the accelerating effect of the built-in electric field on high-energy exciton separation and carrier transfer. In addition to accelerating exciton decay, the electric field optimizes carrier transport pathways, achieving an EQE of up to 98% and a responsivity of 286 mA·W^{-1}. The WS_2/GaN heterojunction device exhibits a responsivity of 77 mA/W and an EQE of 36%, while the MoS_2/β-Ga_2O_3

heterojunction demonstrates a responsivity of 60 mA/W and an EQE of 21%. In contrast, the built-in electric field of the Schottky junction effectively suppresses non-radiative recombination of high-energy C excitons and optimizes carrier transport pathways, achieving 2- to 4-fold enhancements in EQE and responsivity compared to conventional heterojunctions. Notably, devices with a built-in electric field constructed via a Schottky structure outperform previously reported van der Waals heterojunction designs and avoid the impact of interfacial dangling bonds on performance. This optimization strategy, based on the C-exciton recombination relaxation pathway to accelerate carrier separation and extraction, provides a new approach for exploring the performance of TMDs materials in ultraviolet detection.

Another notable example involves driving C-exciton separation in WS_2 via a strong built-in electric field, enabling rapid carrier transfer and participation in graphene-mediated carrier multiplication (CM), thereby further enhancing the UV light response and EQE.[100] Self-powered solar-blind UV photodetectors, designed through the synergistic interaction of multiple modulation mechanisms, have achieved a high responsivity of 77 mA/W and an EQE of 36% in the solar-blind UV range. This optimization strategy, centered on the carrier relaxation process of high-energy C-excitons, provides broader options for developing UV photodetector performance based on individual 2D TMDs. In summary, high-energy C-excitons not only exhibit significant UV light absorption coefficients but also provide critical insights for improving optoelectronic device performance due to their efficient modulation mechanisms. However, research on high-energy excitons in TMD-based optoelectronic devices remains limited, suggesting considerable potential for advancing the performance of UV optoelectronic devices.

3.3. A strain probe based on high-energy excitons

For atomically thin 2D TMDs materials, the flexible lattice exhibits a significant capacity to withstand external strain. Strain engineering has emerged as an effective approach for modulating material properties and device performance, including bandgap tuning,[101] carrier transport,[102] and electron–phonon coupling.[103] The strong exciton effects in 2D TMDs facilitate precise measurement of both the magnitude and direction of strain, particularly the nonlinear SHG characteristic peaks, which have been demonstrated to exhibit high sensitivity to the resonance energy of high-energy exciton regions with band nesting.[82,84,88]

Khan *et al.* demonstrated that the SHG response induced by high-energy C-exciton resonance in WS_2 is sensitive to folding angles and strain levels.[104] Changes in SHG characteristic peaks enable dynamic monitoring of folding and strain levels in monolayer and few-layer WS_2. As shown in Fig. 9(a), the wavelength-dependent SHG intensity variations in folded monolayer (1L) and wrinkled five-layer (5L) strained WS_2 demonstrate that the SHG intensity in folded regions is generally enhanced under different wavelength excitations. This enhancement is independent of high-energy exciton resonance. In contrast, C-exciton resonance under strain governs the SHG intensity, while the SHG intensity in non-resonant regions is significantly suppressed. The significant nonlinear optical response due to band nesting is confirmed during the straining process. For monolayer WS_2, the SHG intensity exhibits significant variation between folded and unfolded regions, while the peak position remains largely unchanged, a phenomenon attributed to the interlayer coupling in the folded-angle region. For compressive strain, as the strain degree increases from -1.72% to -2.38% in the vertical direction, the SHG peak blue-shifts. The direct bandgap transition increases the C-exciton resonance energy, and the energy change of SHG reveals the strain sensitivity of high-energy excitons (Fig. 9(b)). Furthermore, compressive and tensile strains exhibit distinct tuning effects on the C-exciton resonance peak. Compressive strain leads to an increase in C-exciton excitation energy and a slight decrease in the peak intensity of nonlinear polarizability, while tensile strain results in a decrease in energy and an enhancement in the peak intensity of nonlinear polarizability. This demonstrates the strain-dependent changes in the intensity of SHG peaks (Fig. 9(c)). As shown in Fig. 9(d), the strain fitting slope obtained from density functional theory (DFT) calculations is consistent with experimental values and shows a linear relationship, verifying the predictability and controllability of strain modulation. A non-contact optical measurement method for nanoscale strain can be realized by monitoring the characteristic peaks of C-exciton resonance, facilitating the feasibility of quantitative strain modulation.

Mennel *et al.* systematically investigated the band nesting effects of high-energy C-excitons and strain-induced nonlinear optical measurements in various TMDs materials through a combination of theoretical and experimental approaches, demonstrating the universality of high-energy exciton-based strain probes in 2D TMDs materials.[105] As shown in Fig. 9(e), for tensile strain, although the SHG response curves of MoS_2 and $MoSe_2$ both undergo redshifts at C-exciton energy resonance, the band nesting region of $MoSe_2$ is more dispersed, and the SHG response exhibits the opposite trend compared to MoS_2. By employing the three-point bending technique on a flexible substrate, specific directional high-precision tensile strain can be applied to monolayer TMDs, and the angular-resolved mode of SHG can be determined by measuring the lattice space group and strain-induced structural disruption (Fig. 9(f)). Quantitative analysis of symmetry breaking in SHG signals under uniaxial strain can be performed using the distortion parameter D, the relationship can

be expressed as

$$D = \frac{(A+B)^2}{(A-B)^2} \tag{1}$$

in this context, A represents the contribution from the material maintaining symmetry under strain, while B represents the contribution from symmetry breaking under strain. When $D > 1$, the SHG signal in the strain direction is enhanced; conversely, when $D < 1$, the SHG signal perpendicular to the strain direction is enhanced. Measuring the D value can flexibly and accurately reflect strain distribution, which is applicable to the different response trends between MoS_2 and $MoSe_2$. As shown in Fig. 9(g), the total SHG signal intensity I^{tot} in MoS_2 reaches a peak near the high-energy C-exciton resonance excitation energy, and strain causes the peak to redshift and alter in amplitude. The D value increases from 1 to 2.5 with increasing strain, and the angular-resolved SHG maximum significantly enhances along the tensile strain direction. This originates from the high sensitivity of the JDOS in band nesting to minor strains. The contribution intensity of different K points in the Brillouin zone to the distortion parameter D confirms the dominant role of the Γ point in the distortion degree of MoS_2 (Fig. 9(h)). After applying 1% uniaxial strain, the characteristic peak redshift corresponds to a reduction in the bandgap, a decrease in JDOS, and a weakening of SHG resonance intensity. The localized JDOS singularities in MoS_2 trigger drastic changes in SHG intensity, and the significant increase in the distortion parameter reflects the sensitivity of the SHG response to strain. Notably, compared to traditional strain measurement methods (e.g., AFM for monitoring strain magnitude and electron microscopy for reflecting strain direction),[101,104] SHG measurement can simultaneously monitor both strain magnitude and direction, offering greater efficiency and flexibility. Moreover, the SHG strain sensitivity based on high-energy C-excitons ($\delta_1/\sigma_1 \approx 3.5$) far exceeds the sensitivity of traditional Raman and PL ($\delta_1/\sigma_1 \approx 0.04$). In summary, SHG combined with high-energy exciton resonance and band nesting represents a universal and highly sensitive strain detection technology. Thus, developing nanodevices based on SHG holds broad application prospects in real-time strain monitoring and quantum sensing.

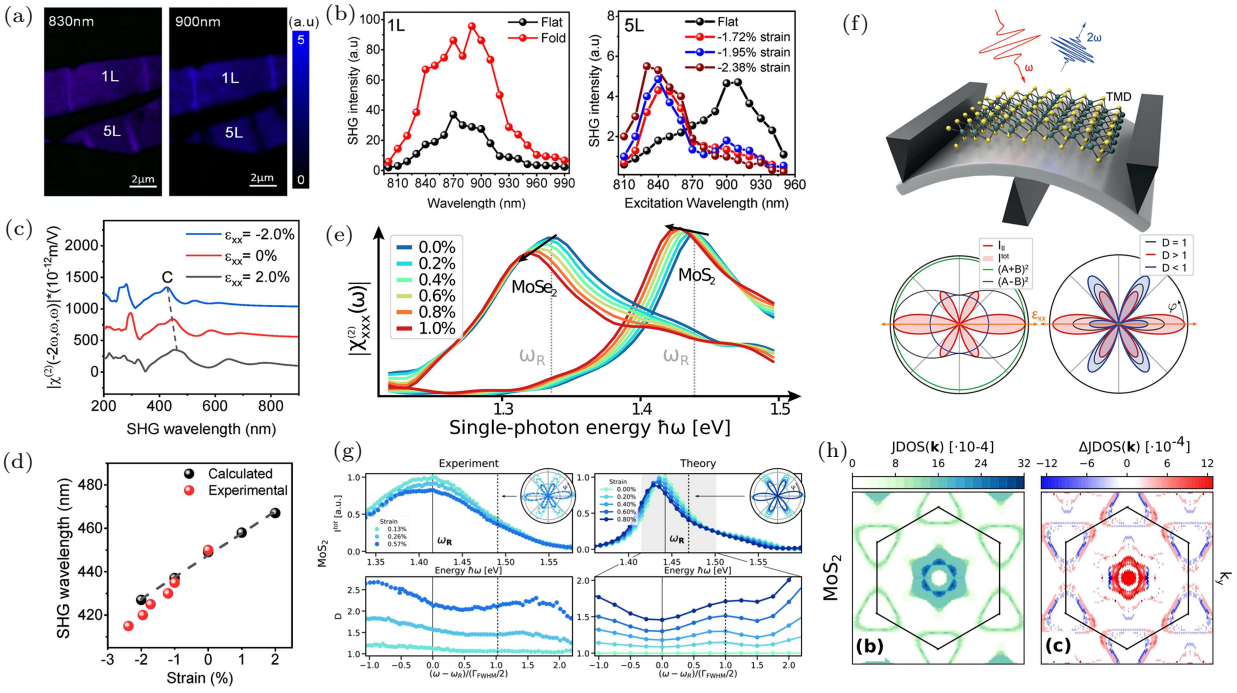


Fig. 9. (a) SHG intensity mapping of 1L folding and 5L wrinkling under 830 nm and 900 nm excitation.[104] (b) Wavelength-dependent SHG intensity curves for 1L and 5L strained regions and flat areas.[104] (c) Wavelength-dependent curves of second-order nonlinear susceptibility under different strains.[104] (d) The relationship between strain and SHG peak shift: a comparison of experimental data and DFT calculation results.[104] (e) Theoretical calculation of the SHG response of MoS_2 and $MoSe_2$ under tensile strain.[105] (f) Experimental setup based on three-point bending technique and distribution diagram of SHG polarization dependence.[105] (g) Comparison of experimental data with theoretical data, revealing the variation of the total SHG intensity (I^{tot}) and distortion parameter D of MoS_2 with strain.[105] (h) The JDOS distribution of unstrained MoS_2 and the ΔJDOS changes after 1% strain.[105]

3.4. An nearly perfect light absorber based on high-energy excitons

For optoelectronic devices dependent on light absorption, developing material systems with near-unity light absorption is essential for advancing high-performance optical communication, green energy harvesting, and photonic sensing technologies.[105,106] In 2D TMDs, heterocavity architectures combining multilayer structures with metallic mirrors can dramatically enhance light–exciton interactions, enabling near-perfect optical absorption efficiencies. For example, Ep-

stein *et al.* designed an asymmetric Fabry–Pérot cavity composed of WS_2, hexagonal boron nitride (h-BN), and an Au mirror. Through optimized structural design, this hybrid cavity achieved nearly 100% excitonic light absorption efficiency in monolayer WS_2 — far surpassing the $\sim 30\%$ absorption limit of conventional monolayer TMDs — demonstrating the superior light-trapping capabilities enabled by resonant amplification via metallic reflectors.[107]

In 2D TMDs materials, the nested band structure between the valence and conduction bands, which hosts high-energy excitons, results in exceptional light absorption efficiency and an optical conductivity that far surpasses traditional 2D semiconductors. While the layered stacking of TMDs shows promise for near-ideal light absorption, actual efficiency is limited, primarily due to interlayer electronic coupling. Using EELS and DFT calculations, Woo *et al.* explored how twisting angles in bilayer WSe_2 affect interlayer coupling and the band structure of high-energy C-excitons.[108] As the twist angle increases, interlayer coupling weakens, seen in the C-exciton peak blue-shifting, with the indirect bandgap peaking at a 30° twist. This weakening arises from the upward shift of the conduction band bottom at the Q point in the bilayer band structure, which enhances the band nesting effect and promotes optical transitions associated with C-excitons. The sensitivity of interlayer coupling strength in high-energy C-excitons to twist angles in bilayer TMDs is highly advantageous for modulating optical absorption efficiency.

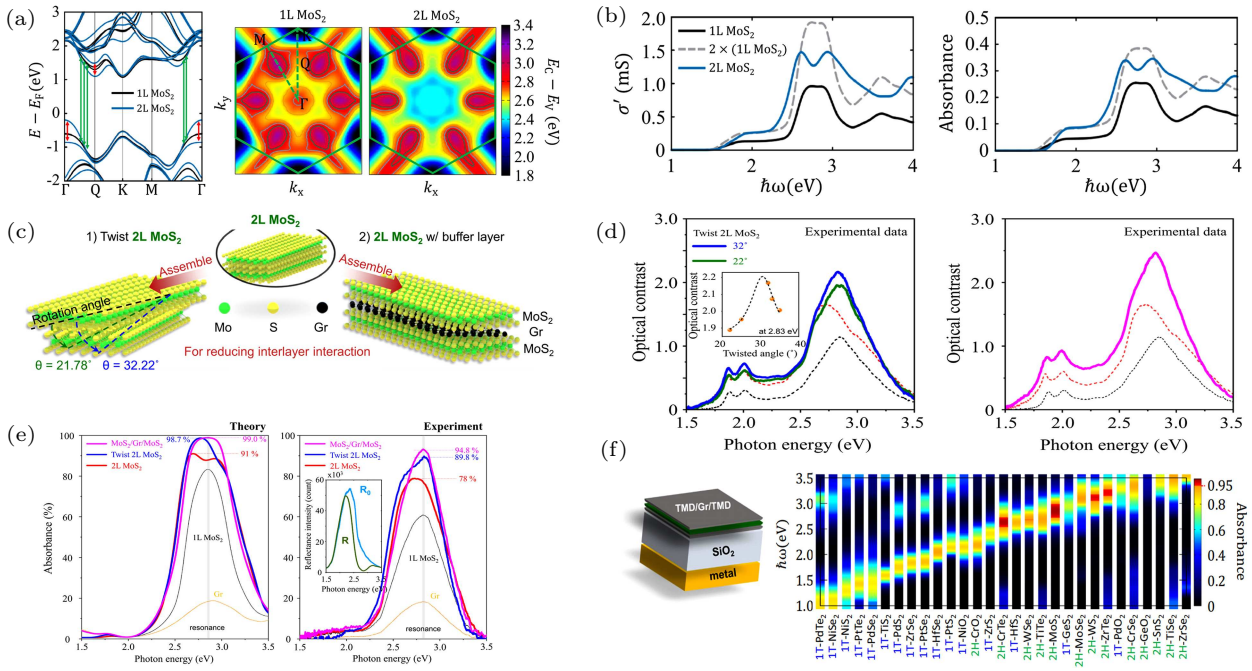


Fig. 10. (a) Comparison of the electronic band structures between monolayer (1L) and bilayer (2L) MoS_2, as well as the distribution of energy band nesting regions in momentum space.[109] (b) Comparison of the optical conductivity σ' and absorbance A between monolayer and bilayer MoS_2.[109] (c) Two strategies for suppressing interlayer coupling in bilayer TMDs: lattice distortion and the insertion of a buffer layer.[109] (d) In the case of experimental measurements, the optical contrast of twisted bilayer MoS_2 is compared with the optical contrast of bilayer MoS_2 that is separated by a graphene (Gr) buffer layer.[109] (e) Comparison of theoretical and experimental absorbance for different MoS_2 structures when combined with a Salisbury screen.[109] (f) Theoretical calculation of the absorbance of various TMD materials in structures containing buffer layers.[109]

Recently, Lee *et al.* proposed an effective strategy to suppress interlayer coupling in atomically thin bilayer TMDs and enhance light absorption efficiency by integrating high-energy exciton band characteristics with an optical resonant cavity (Salisbury screen) structure, achieving near-perfect light absorption.[109] Monolayer and bilayer MoS_2 exhibit distinct differences in electronic band structure and momentum space distribution (Fig. 10(a)). Interlayer coupling in bilayers causes energy shifts at the valence band Γ point and conduction band Q point, weakening band nesting features. The nested band region near the Γ point in the first Brillouin zone is significantly reduced in bilayers, enlarging the energy gap between bands and fragmenting the momentum space for optical transitions. Optical conductivity and absorption, measured to be lower than ideal additive values in bilayers (Fig. 10(b)), confirm the impact of reduced band nesting. Thus, suppressing interlayer coupling is key to restoring band nesting and enhancing light absorption. Two effective strategies for this are twisting bilayer TMDs and inserting a graphene buffer layer (Fig. 10(c)). Increasing the twist angle enlarges the interlayer distance and reduces direct sulfur atom overlap, while the buffer layer provides physical separation, stabilizing the band structure. Optical contrast measurements verify the twist-angle-dependent absorption (Fig. 10(d)). At 32° twist angle, the C-exciton peak redshifts (?? blueshifts) from 2.71 eV (0°) to 2.82 eV, showing suppressed interlayer coupling and enhanced absorption, consistent with previous findings. Compared to twisted bilayers, the buffer layer strategy employs a MoS_2/Gr/MoS_2

heterojunction. After insertion, the C-exciton peak stabilizes, band nesting is preserved, and optical contrast increases by 48%, surpassing untwisted bilayers and monolayers. Combined with a Salisbury screen of SiO_2/Ag reflectors, all structures show unchanged peak positions, but resonance significantly amplifies high-energy exciton absorption peak intensity, reaching 99% theoretical and 94.8% experimental absorption (Fig. 10(e)), confirming the screen's light field localization enhancement. Additionally, the buffer layer's band nesting restoration mechanism is universal across various TMDs (e.g., MoS_2, $CrTe_2$, WS_2), as shown in Fig. 10(f), with significant improvements in absorption efficiency. This simple structural optimization, compared to complex nanofabrication, is more efficient, cost-effective, and scalable. Fully leveraging and optimizing high-energy exciton mechanisms in TMDs represents a new approach for designing efficient light absorbers, expanding applications for next-generation nanoscale atomically thin optoelectronic devices.

4. Conclusion and perspectives

This review comprehensively examines the physics of high-energy excitons in TMDs, focusing on their structure, properties, and applications. The unique electronic structure of high-energy excitons in 2D TMDs, characterized by band nesting, significantly enhances light–matter interactions, creating a sensitive and tunable excitonic platform for advanced optoelectronic devices. As discussed, high-energy excitons excel in several domains: 1) Broad-spectrum absorption: High-energy excitons enable coverage of the visible to UV spectrum, broadening the spectral response of optoelectronic devices. Modulating nanoscale interlayer structures can achieve uniform light absorption efficiency, beneficial for green energy and optical sensors. Their sensitivity to UV light, combined with built-in electric fields that facilitate efficient photogenerated carrier separation, enhances the potential of TMDs in solar-blind UV detection. 2) Nonlinear optical responses: High-energy excitons show strong nonlinear optical responses under resonant excitation, making them ideal for ultrafast optical modulators and communication devices. SHG depends on interlayer coupling and strain levels, and the band nesting effect in TMDs presents promising opportunities for nanoscale strain and biosensing applications, particularly in flexible and wearable devices. 3) Thermal carrier relaxation: High-energy C-excitons have a slow thermal carrier relaxation process, reducing energy loss and enabling efficient carrier extraction and utilization, a significant advantage over traditional semiconductors. This distinctive property holds potential for advancing research in photocatalysis, energy conversion, photovoltaic optimization, and quantum coherence control. Furthermore, constructing heterojunctions or employing interface engineering can establish carrier recirculation channels, potentially suppressing nonradiative recombination and improving device stability and photoelectric conversion efficiency. High-energy exciton research not only deepens our fundamental understanding of 2D TMDs but also serves as a strategic driving force for the revolution in next-generation optoelectronic devices. High-energy excitons can endow strain sensors on flexible substrates with atomic-scale spatial resolution and millisecond-level dynamic response capabilities, providing revolutionary solutions for intelligent bionic skins and micro-electromechanical systems. Through machine learning-assisted band engineering and atomic-level interface manipulation, it is anticipated that directional tailoring of high-energy exciton functionalities can be achieved in three-dimensional heterogeneous integration and on-chip photonic systems. These breakthroughs will propel TMDs from laboratory research to industrial applications, reshaping the future landscape of photonics, quantum information, and green energy technologies.

High-energy exciton properties, as an emerging research direction in two-dimensional TMDs, are still in a phase of rapid development while facing numerous challenges. The band-nesting effects in different TMDs materials vary in their response to strain, and the nanoscale control of strain distribution is complex. Additionally, the inevitable sulfur/selenium vacancy defects in the growth process of TMDs lead to varying degrees of localization of excitons, which severely affects the carrier dynamics of high-energy excitons and reduces device performance. Additionally, the observed low photoluminescence efficiency under ultraviolet excitation correlates strongly with nonradiative recombination pathways of photoinduced hot carriers in high-energy excitons, necessitating the development of more effective optimization strategies to enhance the conversion of high-energy excitons to band-edge excitons. To address these challenges, we propose the following approaches: The issue of defect density in TMDs can be addressed by introducing passivation layers through atomic layer deposition to suppress defect-mediated nonradiative recombination. Simultaneously, the development of novel in-situ strain detection techniques based on SHG, such as combining DFT calculations with machine learning to optimize the precision of measurement processes at the nanoscale, is warranted. Furthermore, optimizing the construction of more efficient heterostructure interface engineering is a valid strategy for improving light emission efficiency under high-energy excitation. It is noteworthy that external control, such as magnetic fields or polarized light, facilitates the synergistic utilization of multiple exciton states in TMDs, and the exploration of novel radiative recombination channels to improve emission efficiency warrants further investigation. In summary, as a fundamental excitonic characteristic of 2D TMDs, research on high-energy excitons has evolved from fundamental physics to

device applications. The future holds promising opportunities for collaborative innovation in detection technologies, interface engineering design, and theoretical simulations based on high-energy excitons, which could unlock their full potential in quantum technology, energy conversion, and flexible electronic sensing applications.

Acknowledgements

Project supported by the National Natural Science Foundation Fund for Distinguished Young Scholars (Grant No. 52025022), the National Natural Science Foundation of China (Grant Nos. 62574038, 12474421, 62275045, and 12074060), the National Key R&D Program of China (Grant No. 2023YFB3610200), and the Fund from Jilin Province (Grant Nos. JJKH20241413KJ and 20240601049RC).

References

[1] Novoselov K S, Geim A K, Morozov S V, Jiang D E, Zhang Y, Dubonos S V, Grigorieva I V and Firsov A A 2004 *Science* **306** 666
[2] Britnell L, Gorbachev R, Jalil R, Belle B, Schedin F, Mishchenko A, Georgiou T, Katsnelson M, Eaves L and Morozov S 2012 *Science* **335** 947
[3] Zhong Y, Yue S, Liang J, Yuan L, Xia Y, Tian Y, Zheng Y, Zhang Y, Du W, Li D, Chen S, Pan A and Liu X 2025 *Nano Lett.* **25** 5274
[4] Coker K, Zheng C, Arhin J R, Agyekum K O B O and Zhang W 2024 *Chin. Phys. B* **33** 037102
[5] You Y, Zhang X X, Berkelbach T C, Hybertsen M S, Reichman D R and Heinz T F 2015 *Nat. Phys.* **11** 477
[6] Bertolazzi S, Krasnozhon D and Kis A 2013 *ACS Nano* **7** 3246
[7] Chen P Y, Quan Z and Wang S D 2024 *Chin. Phys. B* **33** 107105
[8] Zhang Y, Chang T R, Zhou B, Cui Y T, Yan H, Liu Z, Schmitt F, Lee J, Moore R and Chen Y 2014 *Nat. Nanotechnol.* **9** 111
[9] Bao X, Shi J, Han X, Wu K, Zeng X, Xia Y, Zhao J, Zhang Z, Du W, Yue S Wu X, Wu B, Huang Y, Zhang W and Liu X 2025 *Nano Lett.* **25** 2639
[10] Wang G, Chernikov A, Glazov M M, Heinz T F, Marie X, Amand T and Urbaszek B 2018 *Rev. Mod. Phys.* **90** 021001
[11] Zhen B, Hsu C W, Lu L, Stone A D and Soljačić M 2014 *Phys. Rev. Lett.* **113** 257401
[12] Kim J, Hong X, Jin C, Shi S F, Chang C Y S, Chiu M H, Li L J and Wang F 2014 *Science* **346** 1205
[13] Wu Y C, Taniguchi T, Watanabe K and Yan J 2023 *ACS Nano* **17** 15641
[14] Barré E, Karni O, Liu E, O'Beirne A L, Chen X, Ribeiro H B, Yu L, Kim B, Watanabe K and Taniguchi T 2022 *Science* **376** 406
[15] Brotons-Gisbert M, Baek H, Molina-Sánchez A, Campbell A, Scerri E, White D, Watanabe K, Taniguchi T, Bonato C and Gerardot B D 2020 *Nat. Mater.* **19** 630
[16] Shi Q, Shih E M, Rhodes D, Kim B, Barmak K, Watanabe K, Taniguchi T, Papić Z, Abanin D A and Hone J 2022 *Nat. Nanotechnol.* **17** 577
[17] Tan Q, Rasmita A, Li S, Liu S, Huang Z, Xiong Q, Yang S A, Novoselov K and Gao W B 2021 *Sci. Adv.* **7** eabh0863
[18] Hao K, Specht J F, Nagler P, Xu L, Tran K, Singh A, Dass C K, Schüller C, Korn T and Richter M 2017 *Nat. Commun.* **8** 15552
[19] Lindlau J, Selig M, Neumann A, Colombier L, Förste J, Funk V, Förg M, Kim J and Berghäuser G 2018 *Nat. Commun.* **9** 2586
[20] Schmitt D, Bange J P, Bennecke W, Meneghini G, AlMutairi A, Merboldt M, Pöhls J, Watanabe K, Taniguchi T and Steil S 2025 *Nat. Photonics* **19** 187
[21] Li D, Trovatello C, Dal Conte S, Nuß M, Soavi G, Wang G, Ferrari A C, Cerullo G and Brixner T 2021 *Nat. Commun.* **12** 954
[22] Miller B, Lindlau J, Bommert M, Neumann A, Yamaguchi H, Holleitner A, Högele A and Wurstbauer U 2019 *Nat. Commun.* **10** 807
[23] Lundt N, Klembt S, Cherotchenko E, Betzold S, Iff O, Nalitov A V, Klaas M, Dietrich C P, Kavokin A V and Höfling S 2016 *Nat. Commun.* **7** 13328
[24] Sun J, Hu H, Zheng D, Zhang D, Deng Q, Zhang S and Xu H 2018 *ACS Nano* **12** 10393
[25] Wolff C and Mortensen N A 2020 *Nat. Commun.* **11** 4039
[26] Zhou Y, Scuri G, Wild D S, High A A, Dibos A, Jauregui L A, Shu C, De Greve K, Pistunova K and Joe A Y 2017 *Nat. Nanotechnol.* **12** 856
[27] Gillen R and Maultzsch J 2016 *IEEE J. Sel. Top. Quantum Electron.* **23** 219
[28] Splendiani A, Sun L, Zhang Y, Li T, Kim J, Chim C Y, Galli G and Wang F 2010 *Nano Lett.* **10** 1271
[29] Carvalho A, Ribeiro R and Castro Neto A 2013 *Phys. Rev. B* **88** 115205
[30] Jones A J, Muzzio R, Majchrzak P, Pakdel S, Curcio D, Volckaert K, Biswas D, Gobbo J, Singh S and Robinson 2020 *Adv. Mater.* **32** 2001656
[31] Dong K, Zhou H, Gao Z, Xu M, Zhang L, Zhou S, Cui H, Wang S, Tao C and Ke W 2024 *Adv. Funct. Mater.* **34** 2306941
[32] Jia T, Zhang J, Zhong W, Liang Y, Zhang K, Dong S, Ying L, Liu F, Wang X and Huang F 2020 *Nano Energy* **72** 104718
[33] Lan W, Wang Y, Singh J and Zhu F 2018 *ACS Photonics* **5** 1144
[34] Lu Y, Chen T, Mkhize N, Chang R J, Sheng Y, Holdway P, Bhaskaran H and Warner J H 2021 *ACS Nano* **15** 19570
[35] Tan Y, Qiao Q, Zhao T, Chang S, Zhang Z, Zang J, Lin C, Shang Y, Yang X and Zhou J 2024 *J. Mater. Sci. Technol.* **190** 200
[36] Tsai H, Nie W, Blancon J C, Stoumpos C C, Asadpour R, Harutyunyan B, Neukirch A J, Verduzco R, Crochet J J and Tretiak S 2016 *Nature* **536** 312
[37] Zhou X, Lu Z, Zhang L and Ke Q 2023 *Nano Energy* **117** 108908
[38] Rarick H, Kala A, Pumulo S, Manna A, Sharp D, Munley C, Xu X and Majumdar A 2024 *ACS Photonics* **11** 4635
[39] Sinelnik A, Lam S H, Coviello F, Klimmer S, Della Valle G, Choi D Y, Pertsch T, Soavi G and Staude I 2024 *Nat. Commun.* **15** 2507
[40] Schaibley J R, Yu H, Clark G, Rivera P, Ross J S, Seyler K L, Yao W and Xu X 2016 *Nat. Rev. Mater.* **1** 16055
[41] Manzeli S, Ovchinnikov D, Pasquier D, Yazyev O V and Kis A 2017 *Nat. Rev. Mater.* **2** 17033
[42] Koitzsch A, Pawlik A-S, Habenicht C, Klaproth T, Schuster R, Büchner B and Knupfer M 2019 *npj 2D Mater. Appl.* **3** 41
[43] Aleithan S H, Livshits M Y, Khadka S, Rack J J, Kordesch M E and Stinaff E 2016 *Phys. Rev. B* **94** 035445
[44] Klots A, Newaz A, Wang B, Prasai D, Krzyzanowska H, Lin J, Caudel D, Ghimire N, Yan J and Ivanov B 2014 *Sci. Rep.* **4** 6608
[45] Low T and Avouris P 2014 *ACS Nano* **8** 1086
[46] Stauber T, Peres N M and Geim A K 2008 *Phys. Rev. B* **78** 085432
[47] Rose A H, Aubry T J, Zhang H and van de Lagemaat J 2022 *Adv. Opt. Mater.* **10** 2200485
[48] Cha S, Ouyang T, Taniguchi T, Watanabe K, Gabor N M and Lui C H 2024 *Nano Lett.* **24** 14847
[49] Huang W, Xiao Y, Xia F, Chen X and Zhai T 2024 *Adv. Funct. Mater.* **34** 2310726
[50] Wang G, Marie X, Gerber I, Amand T, Lagarde D, Bouet L, Vidal M, Balocchi A and Urbaszek B 2015 *Phys. Rev. Lett.* **114** 097403
[51] Le C T, Clark D J, Ullah F, Jang J I, Senthilkumar V, Sim Y, Seong M J, Chung K H, Kim J W and Park S 2017 *ACS Photonics* **4** 38
[52] Shi J, Liang W Y, Raja S S, Sang Y, Zhang X Q, Chen C A, Wang Y, Yang X, Lee Y H and Ahn H 2018 *Laser Photonics Rev.* **12** 1800188
[53] Guo W P, Liang W Y, Cheng C W, Wu W L, Wang Y T, Sun Q, Zu S, Misawa H, Cheng P J and Chang S W 2020 *Nano Lett.* **20** 2857
[54] Xu C, Mao Y, Li K, Wang Z, Liu X, Dong N, Li S Y, Pan A and Wang J 2024 *Adv. Opt. Mater.* **12** 2302407
[55] Manca M, Glazov M M, Robert C, Cadiz F, Taniguchi T, Watanabe K, Courtade E, Amand T, Renucci P and Marie X 2017 *Nat. Commun.* **8** 14927
[56] Plechinger G, Nagler P, Arora A, Schmidt R, Chernikov A, Del Águila A G, Christianen P C, Bratschitsch R, Schüller C and Korn T 2016 *Nat. Commun.* **7** 12715
[57] Shi H, Yan R, Bertolazzi S, Brivio J, Gao B, Kis A, Jena D, Xing H G and Huang L 2013 *ACS Nano* **7** 1072
[58] Camellini A, Mennucci C, Cinquanta E, Martella C, Mazzanti A, Lamperti A, Molle A, De Mongeot F B, Della Valle G and Zavelani-Rossi M 2018 *ACS Photonics* **5** 3363

[59] Kozawa D, Kumar R, Carvalho A, Kumar Amara K, Zhao W, Wang S, Toh M, Ribeiro R M, Castro Neto A H and Matsuda K 2014 *Nat. Commun.* **5** 4543

[60] Li Y, Wu X, Liu W, Xu H and Liu X 2021 *Appl. Phys. Lett.* **119** 051106

[61] Borzda T, Gadermaier C, Vujicic N, Topolovsek P, Borovsak M, Mertelj T, Viola D, Manzoni C, Pogna E A and Brida D 2015 *Adv. Funct. Mater.* **25** 3351

[62] Goswami T, Bhatt H, Babu K J, Kaur G, Ghorai N and Ghosh H N 2021 *J. Phys. Chem. Lett.* **12** 6526

[63] Li M, Fu J, Xu Q and Sum T C 2019 *Adv. Mater.* **31** 1802486

[64] St-Gelais R, Bhatt G R, Zhu L, Fan S and Lipson M 2017 *ACS Nano* **11** 3001

[65] Urcuyo R, Duong D L, Sailer P, Burghard M and Kern K 2016 *Nano Lett.* **16** 6761

[66] Wang L, Wang Z, Wang H-Y, Grinblat G, Huang Y L, Wang D, Ye X H, Li X B, Bao Q and Wee A S 2017 *Nat. Commun.* **8** 13906

[67] Li Y, Shi J, Chen H, Mi Y, Du W, Sui X, Jiang C, Liu W, Xu H and Liu X 2019 *Laser Photonics Rev.* **13** 1800270

[68] Rose A H, Aubry T J, Zhang H, Vigil-Fowler D and van de Lagemaat J 2022 *J. Phys. Chem. C* **126** 8710

[69] Wei X, Wang Z, Wang Z, Lu Y, Ji Q and Liu W 2024 *Nano Lett.* **24** 9269

[70] Tran T X, Jang Y J, Vu V T, Jung C W, Do V D, Jin Y, Lee J, Kim H and Kim J H 2024 *Nano Lett.* **24** 11163

[71] Fan K, Wang H, Ma Z, Liao W A, Zhang W H, Liu C F, Meng S, Tian G and Fu Y S 2024 *J. Am. Chem. Soc.* **146** 33561

[72] Li Z, Zeng Y, Ou Z, Zhang T, Du R, Wu K, Guo Q, Jiang W, Xu Y and Li T 2022 *Nano Res.* **15** 1616

[73] Wang Y, Deng L, Wei Q, Wan Y, Liu Z, Lu X, Li Y, Bi L, Zhang L and Lu H 2020 *Nano Lett.* **20** 2129

[74] Zhang T and Wang J 2021 *ACS Photonics* **8** 2770

[75] Liu H, Wang C, Zuo Z, Liu D and Luo J 2020 *Adv. Mater.* **32** 1906540

[76] Qu J, Wei Y, Zhao L, Tan R, Li W, Shi H, Zhang Y, Yang J, Gao B and Li X 2024 *ACS Nano* **18** 34322

[77] Arora A, Drüppel M, Schmidt R, Deilmann T, Schneider R, Molas M R, Marauhn P, Michaelis de Vasconcellos S, Potemski M and Rohlfing M 2017 *Nat. Commun.* **8** 639

[78] Kumar D, Kumar V, Kumar R, Kumar M and Kumar P 2022 *Phys. Rev. B* **105** 085419

[79] Yang L, Peng Y, Yang Y, Liu J, Huang H, Yu B, Zhao J, Lu Y, Huang Z and Li Z 2019 *Adv. Sci.* **6** 1900310

[80] Lee J U, Kim K, Han S, Ryu G H, Lee Z and Cheong H 2016 *ACS Nano* **10** 1948

[81] Kim K, Lee J U, Nam D and Cheong H 2016 *ACS Nano* **10** 8113

[82] McCreary K M, Phillips M, Chuang H J, Wickramaratne D, Rosenberger M, Hellberg C S and Jonker B T 2022 *Nanoscale* **14** 147

[83] Wang Y, Carvalho B R and Crespi V H 2018 *Phys. Rev. B* **98** 161405

[84] Tan Q H, Sun Y J, Liu X L, Zhao Y, Xiong Q, Tan P H and Zhang J 2017 *2D Mater.* **4** 031007

[85] Bilgin I, Raeliarijaona A S, Lucking M C, Hodge S C, Mohite A D, de Luna Bugallo A, Terrones H and Kar S 2018 *ACS Nano* **12** 740

[86] Cortijo-Campos S, Kung P, Prieto C and de Andres A 2021 *J. Phys. Chem. C* **125** 23904

[87] Trovatello C, Miranda H P, Molina-Sanchez A, Borrego-Varillas R, Manzoni C, Moretti L, Ganzer L, Maiuri M, Wang J and Dumcenco D 2020 *ACS Nano* **14** 5700

[88] Schneider E, Watanabe K, Taniguchi T and Maultzsch J 2024 *Phys. Rev. B* **110** 125431

[89] Yan Z, Poh E T, Zhang Z, Chua S T, Wang X, Wu X, Chen Z, Yang J, Xu Q H and Goh K E J 2020 *ACS Nano* **14** 5946

[90] Feng J, Li Y, Li J, Feng Q, Xin W, Liu W, Xu H and Liu Y 2022 *Nano Lett.* **22** 3699

[91] Li Y, Pan J, Yan C, Li J, Xin W, Zhang Y, Liu W, Liu X, Xu H and Liu Y 2024 *Nano Lett.* **24** 7252

[92] Liu W, Yang X, Wang Z, Li Y, Li J, Feng Q, Xie X, Xin W, Xu H and Liu Y 2023 *Light-Sci. Appl.* **12** 180

[93] Long Z, Zhou Y, Ding Y, Qiu X, Poddar S and Fan Z 2025 *Nat. Rev. Mater.* **10** 128

[94] Li J, Zhou Y, Li Y, Yan C, Zhao X G, Xin W, Xie X, Liu W, Xu H and Liu Y 2024 *ACS Photonics* **11** 4578

[95] Zhuo R, Wu D, Wang Y, Wu E, Jia C, Shi Z, Xu T, Tian Y and Li X 2018 *J. Mater. Chem. C* **6** 10982

[96] Zeng L H, Lin S H, Li Z J, Zhang Z X, Zhang T F, Xie C, Mak C H, Chai Y, Lau S P and Luo L B 2018 *Adv. Funct. Mater.* **28** 1705970

[97] Zhao Z, Wu D, Guo J, Wu E, Jia C, Shi Z, Tian Y, Li X and Tian Y 2019 *J. Mater. Chem. C* **7** 12121

[98] Wang H, Wang W, Zhong Y, Li D, Li Z, Xu X, Song X, Chen Y, Huang P and Mei A 2022 *Adv. Mater.* **34** 2206122

[99] Yan C, Li Y, Li R, Ma R, Li J, Xin W, Liu W, Xu H and Liu Y 2024 *Laser Photonics Rev.* **18** 2400951

[100] Ma R, Ren H, Yan C, Li Y, Li J, Xin W, Liu W, Zhao X G, Yang L and Feng S 2024 *ACS Photonics* **11** 5339

[101] Yu Y, Dong C-D, Binder R, Schumacher S and Ning C Z 2023 *ACS Nano* **17** 4230

[102] Yang S, Chen W, Sa B, Guo Z, Zheng J, Pei J and Zhan H 2023 *Nano Lett.* **23** 3070

[103] Du Q, Zhu C, Yin Z, Na G, Cheng C, Han Y, Liu N, Niu X, Zhou H and Chen H 2020 *ACS Nano* **14** 5806

[104] Khan A R, Liu B, Lu T, Zhang L, Sharma A, Zhu Y, Ma W and Lu Y 2020 *ACS Nano* **14** 15806

[105] Mennel L, Smejkal V, Linhart L, Burgdörfer J, Libisch F and Mueller T 2020 *Nano Lett.* **20** 4242

[106] F. Imani M, Smith D R and del Hougne P 2020 *Adv. Funct. Mater.* **30** 2005310

[107] Epstein I, Terrés B, Chaves A J, Pusapati V V, Rhodes D A, Frank B, Zimmermann V, Qin Y, Watanabe K and Taniguchi T 2020 *Nano Lett.* **20** 3545

[108] Woo S Y, Zobelli A, Schneider R, Arora A, Preuß J A, Carey B J, Michaelis de Vasconcellos S, Palummo M, Bratschitsch R and Tizei L H 2023 *Phys. Rev. B* **107** 155429

[109] Lee S, Seo D, Park S H, Izquierdo N, Lee E H, Younas R, Zhou G, Palei M, Hoffman A J and Jang M S 2023 *Nat. Commun.* **14** 3889